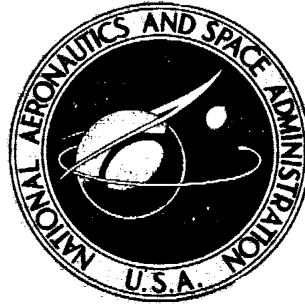


**NASA TECHNICAL
MEMORANDUM**



NASA TM X-3532

NASA TM X-3532

**FLIGHT-MEASURED LIFT AND DRAG
CHARACTERISTICS OF A LARGE, FLEXIBLE,
HIGH SUPERSONIC CRUISE AIRPLANE**

Henry H. Arnaiz

Dryden Flight Research Center

Edwards, Calif. 93523

1. Report No. NASA TM X-3532		2. Government Accession No.		3. Recipient's Catalog No.	
4. Title and Subtitle FLIGHT-MEASURED LIFT AND DRAG CHARACTERISTICS OF A LARGE, FLEXIBLE, HIGH SUPERSONIC CRUISE AIRPLANE				5. Report Date May 1977	
				6. Performing Organization Code	
7. Author(s) Henry H. Arnaiz				8. Performing Organization Report No. H-913	
9. Performing Organization Name and Address NASA Dryden Flight Research Center P. O. Box 273 Edwards, California 93523				10. Work Unit No. 516-51-01	
				11. Contract or Grant No.	
12. Sponsoring Agency Name and Address National Aeronautics and Space Administration Washington, D.C. 20546				13. Type of Report and Period Covered Technical Memorandum	
				14. Sponsoring Agency Code	
15. Supplementary Notes					
16. Abstract <p style="text-align: center;">Flight measurements of lift, drag, and angle of attack were obtained for the XB-70 airplane, a large, flexible, high supersonic cruise airplane. This airplane had a length of over 57 meters (190 feet), a takeoff gross mass of over 226,800 kilograms (equivalent to 500,000 pounds), and a design cruise speed of Mach 3 at an altitude of 21,340 meters (70,000 feet). The performance measurements were made at Mach numbers from 0.72 to 3.07 and altitudes from approximately 7620 meters (25,000 feet) to 21,340 meters (70,000 feet). The measurements were made to provide data for evaluating the techniques presently being used to design and predict the performance of aircraft in this category. Such performance characteristics as drag polars, lift-curve slopes, and maximum lift-to-drag ratios were derived from the flight data. The base drag of the airplane, changes in airplane drag with changes in engine power setting at transonic speeds, and the magnitude of the drag components of the propulsion system are also discussed.</p>					
17. Key Words (Suggested by Author(s)) Flight-measured performance Airplane drag Airplane lift and drag XB-70 airplane				18. Distribution Statement Unclassified - Unlimited Category: 05	
19. Security Classif. (of this report) Unclassified		20. Security Classif. (of this page) Unclassified		21. No. of Pages 62	
				22. Price* \$4.25	

*For sale by the National Technical Information Service, Springfield, Virginia 22161

FLIGHT-MEASURED LIFT AND DRAG CHARACTERISTICS OF A LARGE, FLEXIBLE, HIGH SUPERSONIC CRUISE AIRPLANE

Henry H. Arnaiz
Dryden Flight Research Center

INTRODUCTION

The lift, drag, and angle of attack performance characteristics of the XB-70 airplane were determined from flight measurements. The main purpose of determining these characteristics was to evaluate the techniques presently being used to design and predict the performance of large, flexible, supersonic cruise aircraft. Flight-measured characteristics are especially needed for improving drag prediction techniques, since many aircraft have had problems in this area, especially in the transonic Mach number region. The XB-70 airplane was used for the investigation because its size and speed range was representative of supersonic transport aircraft and because its lift and drag characteristics were subject to the effects of structural flexibility, propulsion system/airframe interactions, and the trim of the airplane. In conjunction with these measurements, a study was made to determine the effects of structural flexibility and other performance-related variables on the overall performance of this airplane for a selected number of actual flight-measured conditions. Reference 1 reports the results of this study, and this paper makes frequent reference to that report.

The data presented in this report were obtained under trimmed conditions at Mach numbers from 0.72 to 3.07 and at altitudes from approximately 7620 meters (25,000 feet) to 21,340 meters (70,000 feet). The data presented include lift, drag, and angle of attack measurements for the XB-70 airplane over this Mach number range. Base drag characteristics, propulsion system drag, and measurements of the effects of engine power changes on airplane drag are also presented.

SYMBOLS

Physical quantities in this report are given in both the International System of Units (SI) and U.S. Customary Units (ref. 2).

A	effective flow area, meters ² (feet ²)
a	acceleration, meters/second ² (feet/second ²)
C_D	drag coefficient
C_{D_0}	minimum drag coefficient of given drag polar
C_L	lift coefficient
D	drag force, newtons (pounds)
F_g	engine gross thrust, newtons (pounds)
F_n	engine net thrust, newtons (pounds)
F_{nt}	airplane net propulsive thrust, newtons (pounds)
F_r	engine ram drag, newtons (pounds)
g	gravitational acceleration, 9.8066 meters/second ² (32.1741 feet/second ²)
L	lift force, newtons (pounds)
L/D	lift-to-drag ratio
$(L/D)_{max}$	maximum lift-to-drag ratio
M	Mach number
\dot{m}	mass flow, kilograms/second (pounds/second)
n_X	accelerometer reading along airplane longitudinal centerline, g 's
n_Z	accelerometer reading normal to airplane centerline (load factor), g 's
p	static pressure, newtons/meter ² (pounds/feet ²)
q	dynamic pressure, newtons/meter ² (pounds/feet ²)
S_w	airplane reference wing area, 585 meters ² (6297 feet ²)
T_t	total temperature, kelvins (degrees Rankine)

V	velocity , meters/second (feet/second)
W	airplane weight , newtons (pounds)
X	longitudinal airplane axis
X'	airplane flightpath axis
Z	axis normal to airplane longitudinal axis
Z'	axis normal to airplane flightpath
α	airplane angle of attack , degrees
α_0	airplane angle of attack at zero lift coefficient, degrees
γ	ratio of specific heat
Δ	incremental change
δ_a	aileron deflection , positive roll to the right , degrees
δ_{byp}	inlet bypass door deflection , degrees
δ_c	canard deflection , positive leading edge up , degrees
δ_e	elevator deflection , positive trailing edge down , degrees
δ_r	rudder deflection , positive trailing edge left , degrees
δ_t	wingtip deflection , positive down , degrees
θ	flightpath angle , degrees
φ	inlet airflow discharge angle , degrees

Subscripts:

byp	inlet bypass system
$meas$	measured
mf	inlet mass flow ratio
y	inlet bypass or boundary layer bleed
∞	free stream

DESCRIPTION OF AIRPLANE AND PROPULSION SYSTEM

The XB-70 airplane was a large, delta-winged supersonic cruise aircraft designed for sustained flight at Mach numbers up to 3 at an altitude of 21,340 meters (70,000 feet). The airplane had a gross takeoff mass in excess of 226,800 kilograms (equivalent to 500,000 pounds) and an empty mass of approximately 124,740 kilograms (equivalent to 275,000 pounds).

Two airplanes were built and designated the XB-70-1 and XB-70-2 airplanes. Figure 1 shows the configuration of the XB-70-1 airplane. The pertinent physical

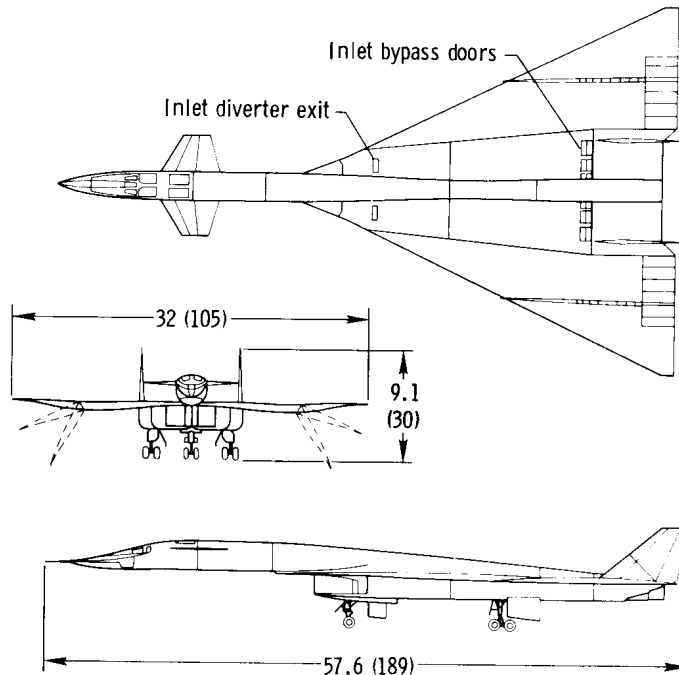


Figure 1. Three-view drawing of XB-70-1 airplane. Dimensions in meters (feet).

characteristics of both airplanes are presented in table 1. The primary difference between the airplane configurations was that the XB-70-1 airplane had a wing dihedral angle of 0° and the XB-70-2 airplane had a wing dihedral angle of 5° . The dihedral, which was produced by inserting a wedge at the root section of the wing, was created to provide greater stability in the roll and yaw axes at high Mach numbers.

The airplane design incorporated a thin wing with a 65.6° leading-edge sweep and downward-folding wingtips for increased high speed stability. The nominal wingtip folding schedule and operating limits are shown in figure 2. The fuselage had a long, slender, cylindrical section forward and above the wing plane. The nose ramp in front of the cockpit had two positions; it was put down for visibility at low speeds and up for wave drag reduction at supersonic speeds.

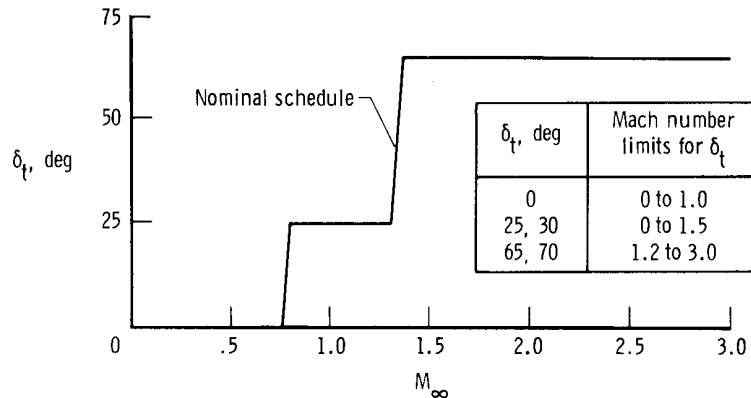


Figure 2. Nominal schedule and operating limits for wingtip positions.

There was a movable low-aspect-ratio canard directly behind the cockpit. The canard had a flap that was deflected during takeoff and landing. In the normal flight configuration, the flap was not deflected and the canard position was geared to the elevons for pitch control in a ratio of $\frac{\delta_c}{\delta_e} = 0.15$; however, some exceptions to these positions were made in flight (ref. 1).

The elevons were split into six spanwise segments on each wing semispan to prevent binding due to wing bending. When the wingtips were deflected, the two outermost elevon segments on each wing were faired (zero deflection) and became part of the folded wingtip. Twin movable vertical stabilizers with inclined hinge lines provided directional stability and control. Figure 3 shows the XB-70 control surfaces and their respective limits.

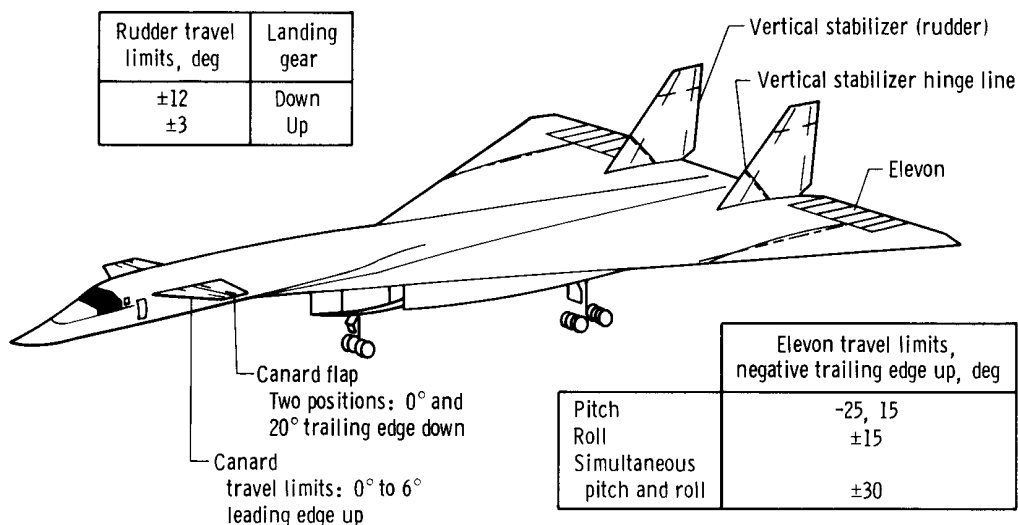


Figure 3. Control surfaces.

As figure 4 shows, the propulsion system, which consisted of the inlet and engines, occupied most of the rear lower fuselage. The inlets were of the two-dimensional mixed-compression type and were designed to operate efficiently at

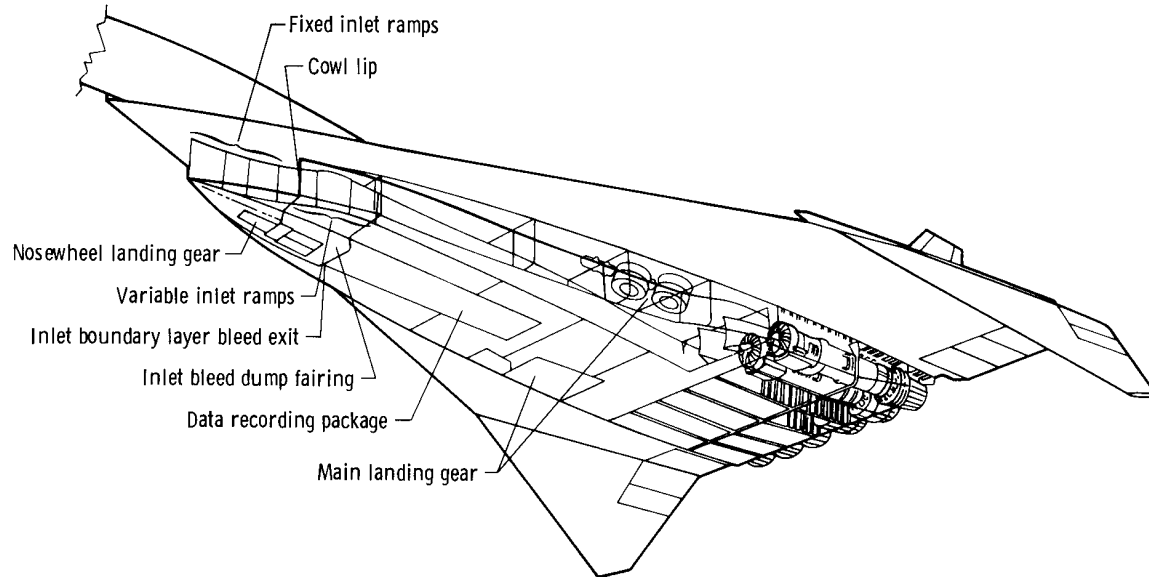


Figure 4. Propulsion system.

high supersonic speeds. Each inlet was equipped with fixed vertical ramps in front of the cowl lip and variable ramps in the region of the throat to control the throat area. There were six bypass doors for each inlet on top of the wing just in front of the engine face between the vertical tails (figs. 1 and 5). The inlet ramps and

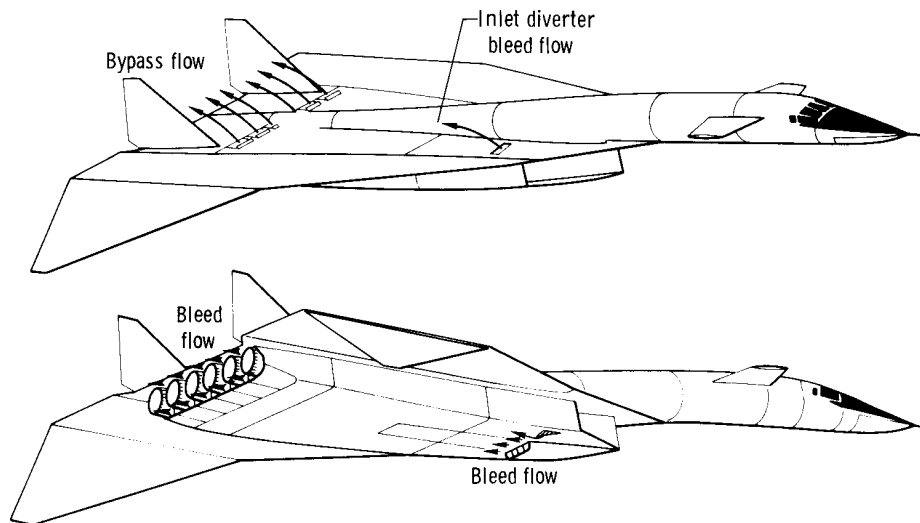
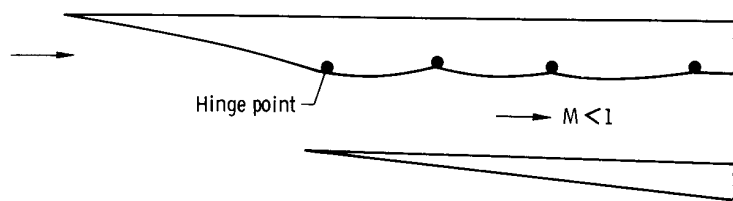
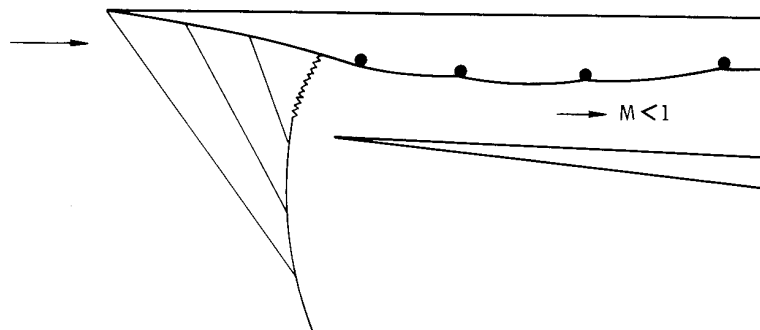


Figure 5. Exits for inlet bypass and boundary layer bleed flow.

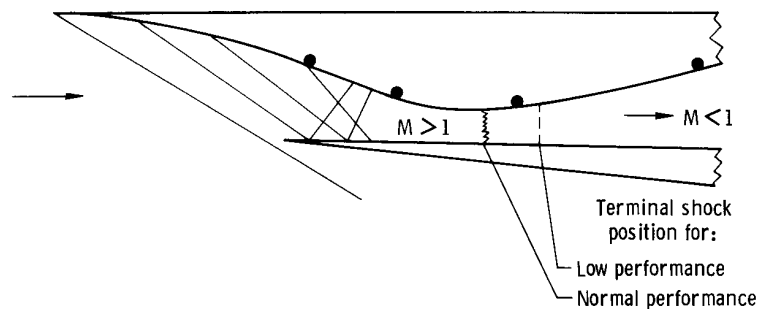
bypass doors were used to optimize the performance of the inlet throughout the speed range. Their operation and the shock systems associated with the inlet are shown schematically in figure 6. At subsonic speeds, the inlet acted as a conventional diffuser. The inlet throat area was at its maximum (fig. 6(a)), and the bypass doors were closed. From Mach 1 to 2, the inlet operated in an external compression mode (fig. 6(b)). The throat size was controlled as a function of inlet Mach number, and the bypass doors were kept open to prevent inlet buzz in the event of an emergency engine shutdown. Above Mach 2, the inlet operated in the mixed-compression mode (fig. 6(c)). Throat area decreased with increasing inlet Mach number to a minimum value at Mach 3. To maximize the performance of the inlet, the bypass doors were positioned to keep the terminal shock wave near the throat.



(a) $M_{\infty} < 1$, bypass doors closed.



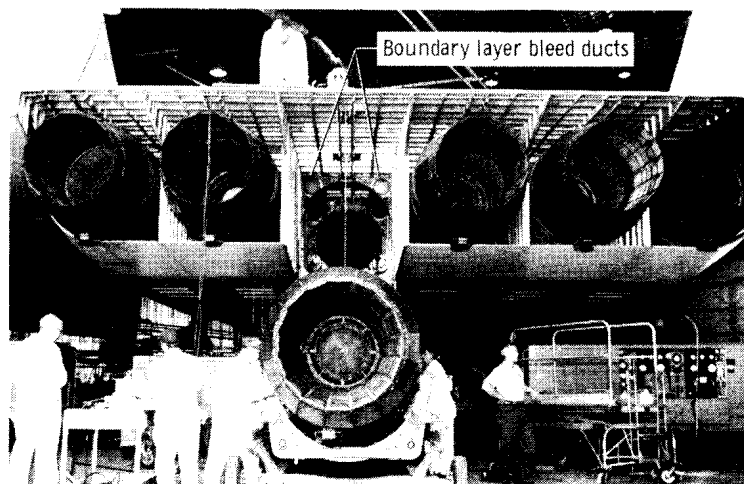
(b) $M_{\infty} = 1$ to 2, bypass doors partially opened, external compression mode.



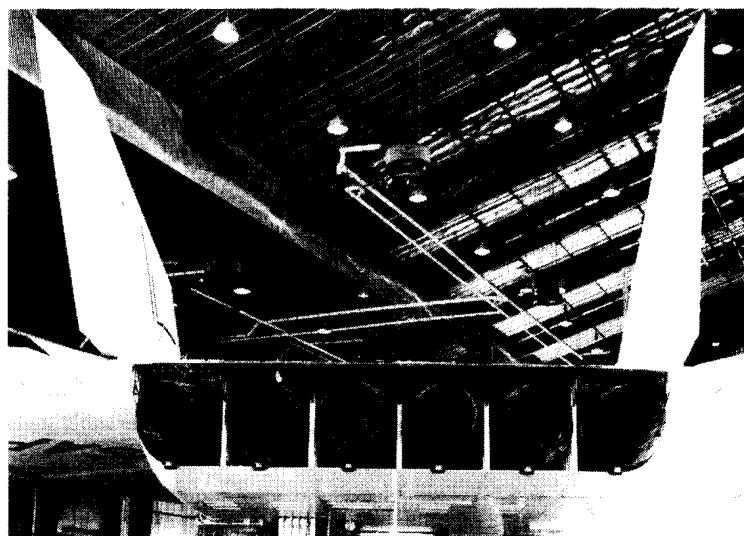
(c) $M_{\infty} > 2$, bypass doors variable, mixed-compression mode.

Figure 6. Modes of inlet operation.

The inlet boundary layer about the inlet throat was bled off to reduce shock-induced boundary layer separation. A two-dimensional ram scoop bled the boundary layer from the ceiling of the duct; this air was ducted through and dumped over the upper surface of the wing through a diverter (figs. 1 and 5). Bleed air near the throat was removed through 8-percent-porosity bleed panels, which were arranged in four zones. Part of this air was dumped underneath the inlet through louvers and a bleed dump fairing with an exit like an aft-facing step (figs. 4 and 5). The rest was ducted through the inlet to the base region of the airplane, increasing the pressure in this region and reducing base drag (figs. 5 and 7). Appendix A describes the inlet bleed and bypass systems in greater detail.



(a) Engine removed showing boundary layer bleed duct exits.



(b) Airplane base region.

E-17194

Figure 7. Airplane base region.

The inlets supplied air to six YJ93-GE-3 afterburning turbojet engines, which were mounted side by side, three engines per inlet, in the rear section of the nacelle. The engines were rated at 133,500 newtons (30,000 pounds) sea level static thrust and had a compressor airflow capability of 120 kilograms per second (264 pounds per second) and an 8.7-to-1 pressure ratio (refs. 3 and 4). Each engine was equipped with an 11-stage axial-flow compressor with variable stators, an annular combustion system, a two-stage air-cooled turbine, and mechanically linked variable-area primary and secondary exhaust nozzles.

The engines exhausted into the airplane's large base region (figs. 5 and 7). This region was divided into compartments that housed the engines and was somewhat unusual in that the upper and lower surfaces of the fuselage terminated at different fuselage stations, causing the engine nozzles to overhang the lower fuselage surface. The base region did not have an aft-facing bulkhead type of surface; the most rearward surface of this type was the engine's rear firewall, which was approximately 4.57 meters (15 feet) in front of the engine's exit plane.

IN-FLIGHT MEASUREMENT SYSTEM

Data Acquisition System

The flight instrumentation consisted of approximately 900 recording data sensors, which were installed throughout the vehicle. Sensor signals were transmitted to a specially designed data recording package housed in the weapons bay of the airplane for signal conditioning, sampling, telemetering, digitizing, and recording. The data were recorded on magnetic tape and processed by a ground-based data reduction facility.

Details of the engine and inlet measurements are given in reference 3, appendix A, and table 2. The data recording package and the reduction facility are discussed in references 5 to 7.

Lift and Drag Measurements

The parameters used to calculate the performance of the XB-70 airplanes and the estimated error or uncertainty in each measurement are listed in table 3. The differences in the measurement precisions for the XB-70-1 and XB-70-2 airplanes resulted from the use of more extensive and sensitive instrumentation in the XB-70-1 airplane. Figure 8, from reference 8, shows the variation of the uncertainties in free-stream Mach number, M_∞ , and free-stream static pressure, p_∞ , with Mach number. Some of the parameters listed in table 3 were obtained from several instruments and from calculations that required other sources of information (ref. 3). For these parameters, the establishment of uncertainties was difficult: Errors from the instruments, the techniques used to make the measurements, and the sources of information required for the calculations can accumulate. For this reason most of the uncertainties in table 3 are only estimated. As discussed later, the results obtained during this investigation indicate that precisions higher than those shown in table 3 may have been obtained.

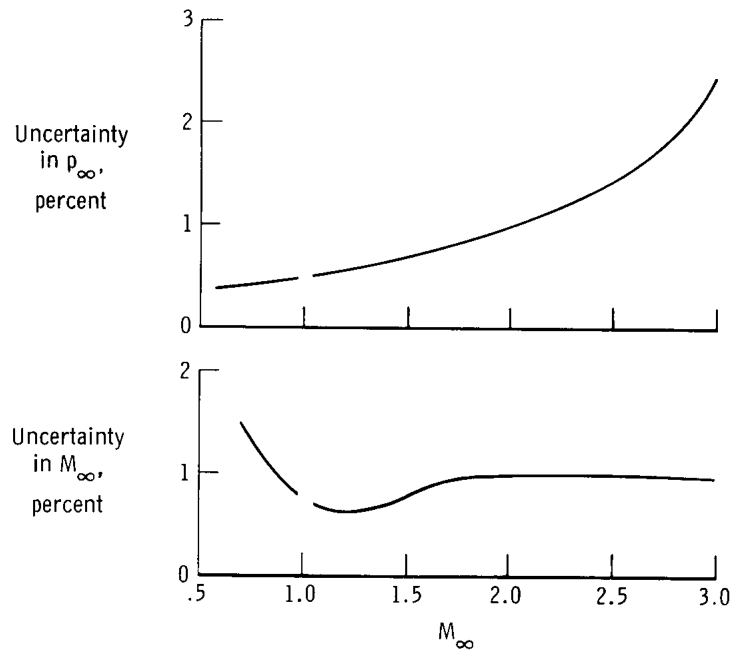


Figure 8. Estimated uncertainty in M_∞ and p_∞ for XB-70-1 and XB-70-2 airplanes (ref. 8).

Nose boom measurements.—Measurements of free-stream Mach number and free-stream static pressure were obtained from calibrated airspeed pitot-static probes that were mounted on the nose boom of the airplane. The techniques used to obtain the measurements are described in reference 8.

The uncertainty in these parameters stems from errors in the pressure-sensing instruments and the position error correction associated with the pitot-static pressure probes. The measurement accuracy is summarized in figure 8.

Aircraft angle of attack was measured by a vane located approximately halfway out on the aircraft nose boom (ref. 8). The precision of the angle of attack measurement was estimated to be $\pm 0.3^\circ$. This estimate was made by combining the instrument errors and the effects of vane float, fuselage bending, boom bending, and pitch velocity. The angle of attack measurements for the subsonic Mach number conditions were also corrected for upwash from the lifting effects of the nose boom, fuselage, canard, and wing. The error due to fuselage bending was not well enough defined to permit a correction to be applied, but reference 1 indicates it to be as great as 0.2° .

Acceleration.—Two accelerometers were used to measure acceleration along the normal and longitudinal axes of the airplane. For the XB-70-1 airplane, two sensitive accelerometers were mounted on locally rigid airplane structure approximately one-third of the way between the center of gravity and the cockpit. The accelerometers were not corrected for the off-center-of-gravity location because this correction was insignificant for the kinds of maneuvers and aircraft pitching accelerations experienced during the tests. For the XB-70-2 airplane, the accelerometers were

close to the center of gravity but lacked the sensitivity of the XB-70-1 accelerometers. The measurement accuracy shown in table 3 represents the accuracy of the instrument only.

Aircraft weight.—The weight of the aircraft in flight was determined by adding the weight of the empty aircraft, that of the consumables (fuel, water, and nitrogen) at the time of interest, and that of the crew. Fuel weight was determined from fuel tank measurements made in the 10 fuel tanks. The weight of the water and nitrogen for a given time was estimated by measuring the quantity of these consumables before and after flight and using a linear interpolation for the flight interval.

The weight measurement was estimated to be accurate within 1.5 percent. The largest source of error was the fuel quantity measurement. The empty weight of the aircraft was known accurately, and the amount of water and nitrogen consumed during the flight was small in comparison with the fuel.

Net propulsive thrust and engine gross thrust.—Net propulsive thrust, F_{nt} , was obtained by subtracting total inlet drag from engine net thrust, F_n (app. A). Engine net thrust was obtained by using a complex computer program to combine engine measurements and known engine operating characteristics, a technique known as the gas generator method. The application of the gas generator method to the YJ93-GE-3 engines and the aircraft instrumentation is described in detail in reference 3. The method used to determine engine gross thrust, which is part of the net thrust calculation, is also described in that reference.

The measurement of the increments of drag due to the aircraft's inlet and the associated instrumentation is described in appendix A.

The accuracy of airplane net propulsive thrust, F_{nt} , and engine gross thrust, F_g , is difficult to establish because it is subject to errors in approximately 300 instrument measurements, the uncertainty of the techniques used in making these measurements, the inherent inaccuracy of using average engine operating characteristics, and the uncertainty in the method used to arrive at a single value from all these elements. To obtain information about the uncertainty of F_{nt} and F_g , a series of ground thrust tests, an in-flight error analysis for a typical Mach 2.5 flight condition, and an in-flight excess thrust comparison were made. The results, which are presented in references 3, 9, and 10, indicate that a precision of 5 percent or better could be expected for net propulsive thrust and 3 percent or better for engine gross thrust for the XB-70-1 airplane. Less precision was expected for the XB-70-2 airplane because the instrumentation was less comprehensive and somewhat less refined than for the XB-70-1 airplane.

Control Surface Deflection Measurements

The deflections of the control surfaces (elevons, ailerons, canards, and rudders) were also measured. A description of these measurements, along with their precision, is given in references 2 and 11.

FLIGHT TEST CONDITIONS AND TECHNIQUES

Figure 9 shows the operational envelope and flight conditions where performance measurements were obtained for both XB-70 aircraft. Table 4(a) lists the flight test

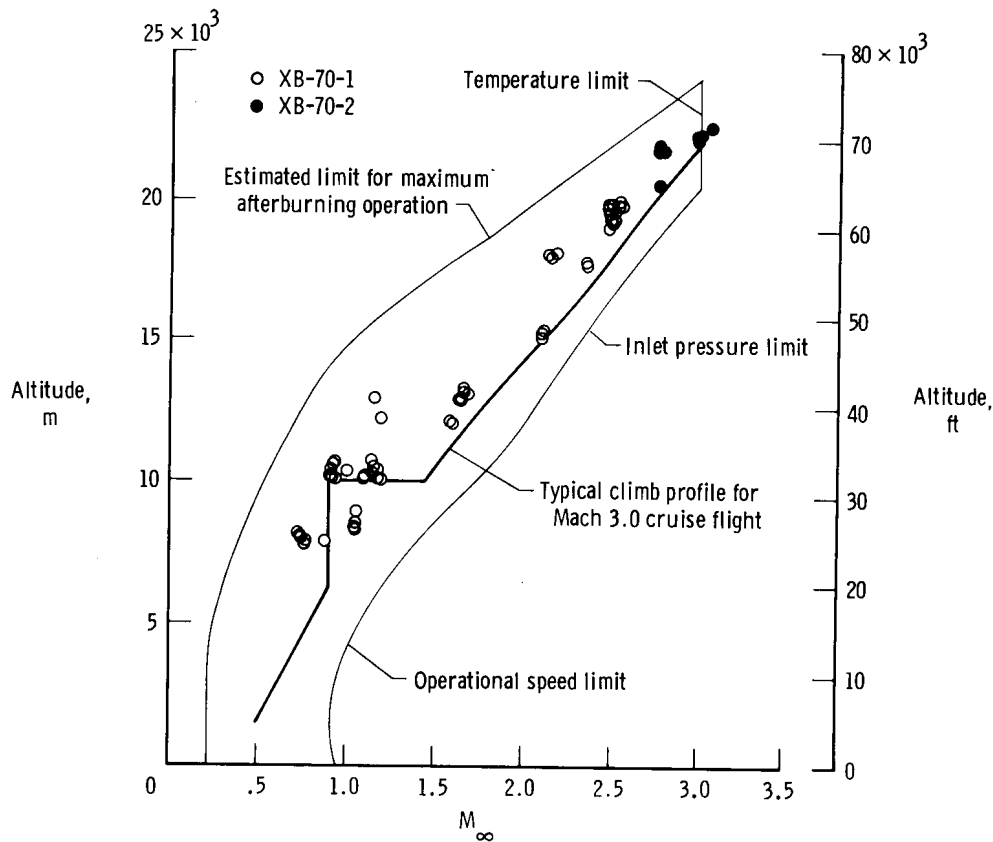


Figure 9. Operational envelope showing flight conditions for performance measurements.

conditions and table 4(b) indicates the aircraft configuration and the values of the parameters used to calculate the lift and drag coefficients.

Three basic maneuvers were used to obtain the performance data: stabilized flight, roller coaster maneuvers, and constant Mach number climbs and descents. Data for the XB-70-2 airplane were acquired only during stabilized flight, because the data were acquired early in the airplane's evaluation, when the airplane could not be flown at conditions far from $1g$.

Stabilized Flight

Most of the performance data were acquired during stabilized flight. Before the data were acquired, an attempt was made to fly at a constant Mach number and altitude for several minutes to stabilize the performance parameters. Time histories were then examined and a time point that was representative of the most stable

portion of the maneuver was chosen. The data in a 2-second interval about this point were averaged and used in the performance calculation process. In the absence of turbulence, stable conditions lasted as long as several minutes; when atmospheric turbulence was encountered, conditions were only quasi-stabilized, sometimes lasting only seconds.

Roller Coaster Maneuvers

The roller coaster maneuver was used to vary lift and drag at a given Mach number. It consisted of stabilizing the airplane at a certain Mach number and altitude and then using pitch control to change angle of attack and normal acceleration at the stabilized altitude in a slow sinusoidal variation. Excursions in normal acceleration near the airplane limits, which were $0.5g$ to $1.5g$, were made in order to generate the largest possible variations in lift and drag. These maneuvers were performed in such a way as to keep Mach number and altitude as constant as possible. The time histories were examined, and the maximum and minimum values of normal acceleration for each cycle were identified. The maximum and minimum values were then used in the performance calculations.

Constant Mach Number Climbs and Descents

Constant Mach number climbs and descents were made primarily to evaluate the accuracy of the thrust measurements, as discussed in reference 10. The maneuver consisted of flying the aircraft through a certain altitude in a constant Mach number climb at the maximum afterburner power setting. Once the specified altitude was crossed, power was reduced to the setting necessary for the airplane to descend at the same Mach number in a stabilized descent through the same altitude point.

The climb/descents were performed over a relatively short time interval to minimize changes in airplane weight and atmospheric conditions.

Only six data points were acquired with these maneuvers (three climbs and three descents). They are identified in table 4.

IN-FLIGHT LIFT AND DRAG MEASUREMENT TECHNIQUE AND ACCURACY

Derivation of Airplane Thrust and Drag

Thrust.—The thrust of the airplane was derived from the forces associated with the inlet mass flow that entered and exited the control volume shown in figure 10. These forces result from the difference between the momentum and pressure of the inlet mass flow stream tube in the free stream in front of the airplane and at the point where the flow exits the propulsion system. To obtain airplane thrust, all the forces, which were determined as described in appendix A, were resolved along the flightpath. The only exception was engine gross thrust.

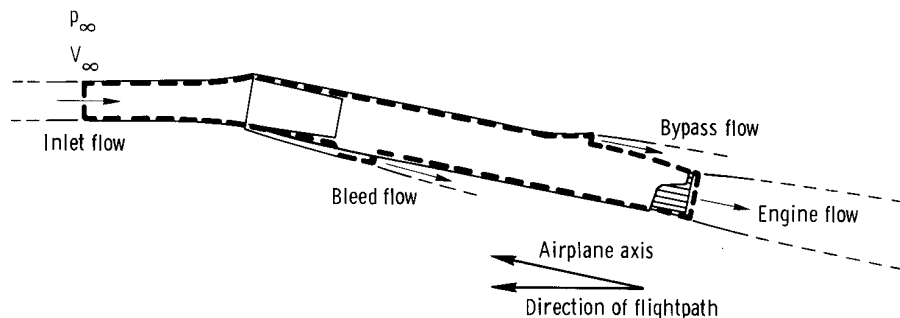


Figure 10. Control volume used to define airplane net propulsive thrust.

The net propulsive thrust, F_{nt} , was used to combine the resultant inlet drag force and the engine gross thrust by way of an algebraic, not a vector, sum. Since the engine gross thrust force is along the longitudinal axis of the airplane and not the flightpath, this approach enabled F_{nt} to be independent of airplane angle of attack. This method of determining the propulsion system forces charged the losses in momentum in the inlet stream tube incurred in crossing the bow and wing leading-edge shock waves of the airplane to the propulsion system. Assigning bow shock losses in this way is normal within the propulsion airframe discipline and is acceptable as long as the same convention is used to treat any wind tunnel model results that are compared with the full-scale data. In the absolute sense, however, the drag coefficients derived from this convention are made larger by the momentum loss incurred in front of the inlet.

The drag components due to the inlet bypass and boundary layer bleed systems can be significant for mixed-compression inlets. Figure 11 shows the size of these components relative to total airplane drag.

The lift components due to the inlet forces were small and were assumed to cancel out.

All other forces related directly or indirectly to the propulsion system were charged to the airplane. These forces included those resulting from the spillage of excess air from the inlet, the pressure on the outside surfaces of the inlet components (such as the bypass doors and bleed dump fairings), and the pressure due to the interaction of the airflows exiting the inlet (such as those from the bypass and boundary layer bleed systems) with the surrounding airstream. The drag associated with the pressure on the large base region of the propulsion system was also charged to the airplane.

Drag.—Airplane drag was defined as the sum of the aerodynamic forces acting on the external surfaces of the aircraft along the direction of and opposite to the flightpath. It included all the drag components due to the propulsion system that were not accounted for otherwise.

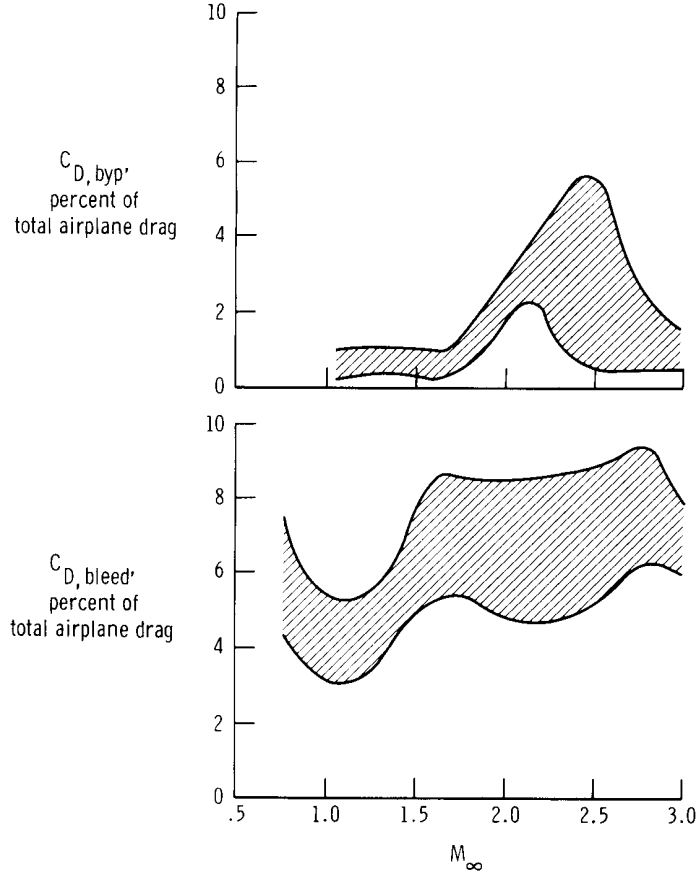


Figure 11. Variation in measured inlet bypass and bleed drag with Mach number for typical 1g flight.

The drag due to the base area of the airplane is made up of drag charged to both the airplane and the propulsion system, because part of the inlet boundary layer air was ducted to this region. The method used to account for the drag in this region was to charge the momentum term of the bleed flow at the exit plane to the propulsion system and the pressure term, or base drag, to the airplane.

Equations for Flight Lift and Drag Coefficients

To calculate the lift and drag coefficients, aircraft accelerations were combined with force, thrust, weight, and airspeed measurements by using the following equations:

$$C_D = \frac{1}{q_\infty S_w} \left[W(n_Z \sin \alpha - n_X \cos \alpha) + F_{nt} - F_g(1 - \cos \alpha) \right] + \Delta C_{D,mf}$$

$$C_L = \frac{1}{q_\infty S_w} \left[W(n_Z \cos \alpha + n_X \sin \alpha) - F_g \sin \alpha \right]$$

where q_∞ is dynamic pressure ($0.5 \gamma p_\infty M_\infty^2$), and S_w is airplane reference wing area (585 square meters (6297 square feet)). These equations are developed in appendix B.

As mentioned previously, the increment of drag due to the spillage of air around the inlet at off-design conditions was charged to airplane drag. At conditions below Mach 2, the inlet did not operate in a mixed-compression mode, however, and this caused the inlet mass flow ratio at a given Mach number to vary from the reference schedule shown in figure 12. The resulting variations in spillage

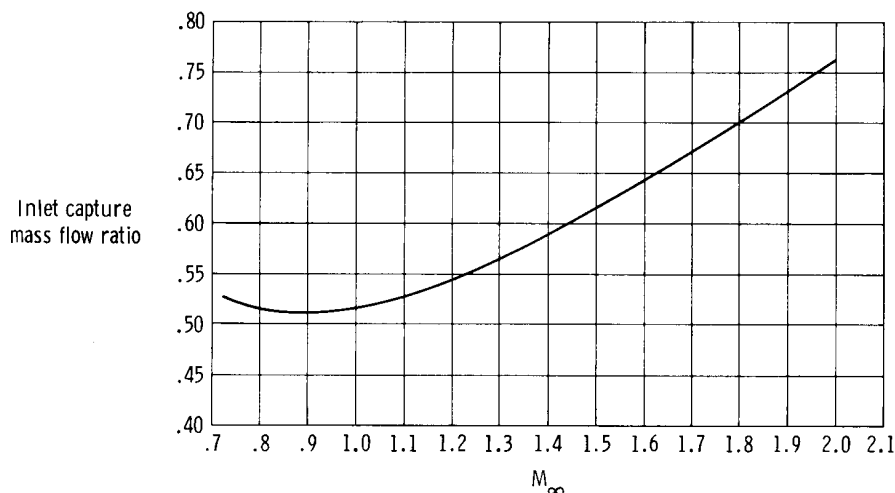
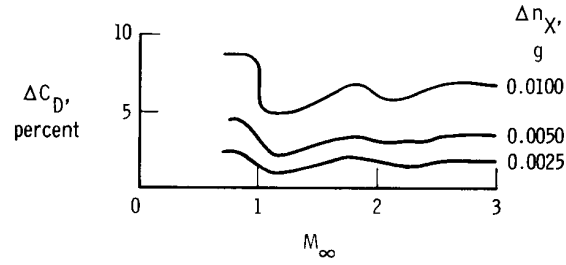


Figure 12. Reference inlet mass flow ratio for XB-70-1 airplane. Based on flight-measured values for nominal flight conditions.

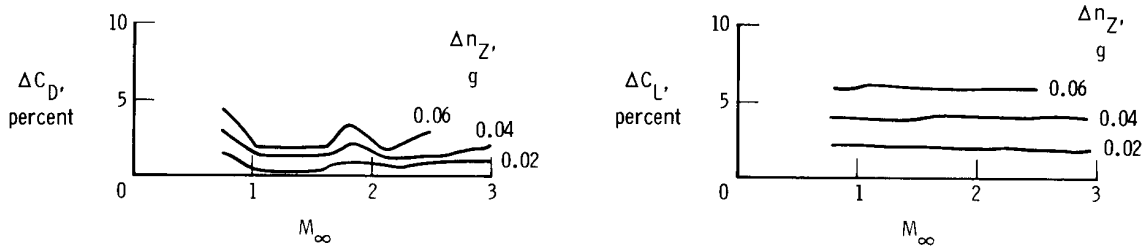
from the inlet caused variations in drag and therefore the drag coefficient, C_D . These variations were removed from C_D values for Mach numbers less than 2 by adding a drag coefficient increment, $\Delta C_{D,mf}$. This increment was obtained from wind tunnel data. For the most part it was less than 1 drag count (a C_D value of 0.0001), and it had a maximum value of 2 drag counts. Above Mach 2, where the inlet operated in a mixed-compression mode, no correction was necessary.

Precision of Lift and Drag Measurements

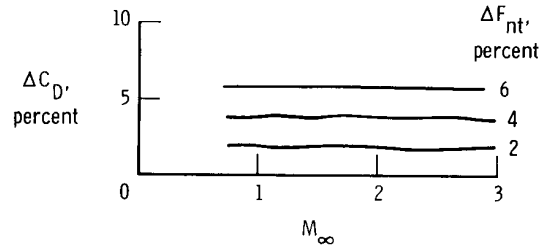
A study was made to determine the sensitivity of C_L and C_D to small errors in the variables that contributed to them. The results of this study are shown in figure 13, in which changes in C_L and C_D are shown as a function of Mach number for errors of various sizes in the measured quantities.



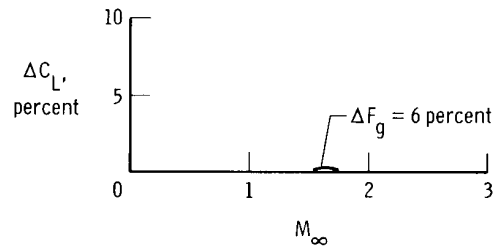
(a) Errors in longitudinal acceleration. For $\Delta n_X = 0.0100$, $\Delta C_L < 0.1$ percent.



(b) Errors in normal acceleration.

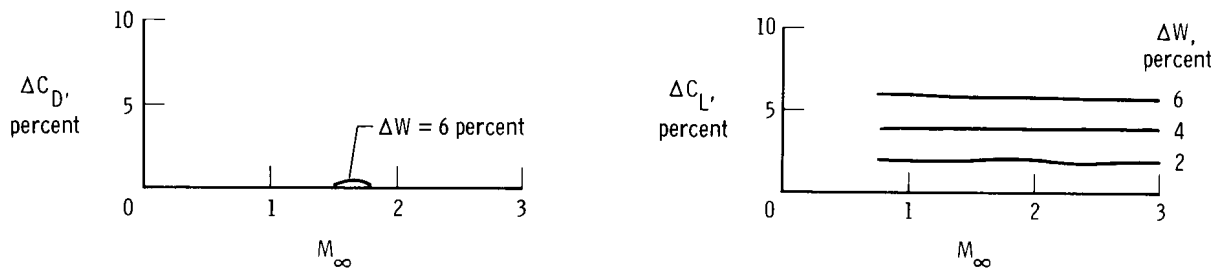


(c) Errors in net propulsive thrust. For $\Delta F_{nt} = 6$ percent, $\Delta C_L < 0.1$ percent.

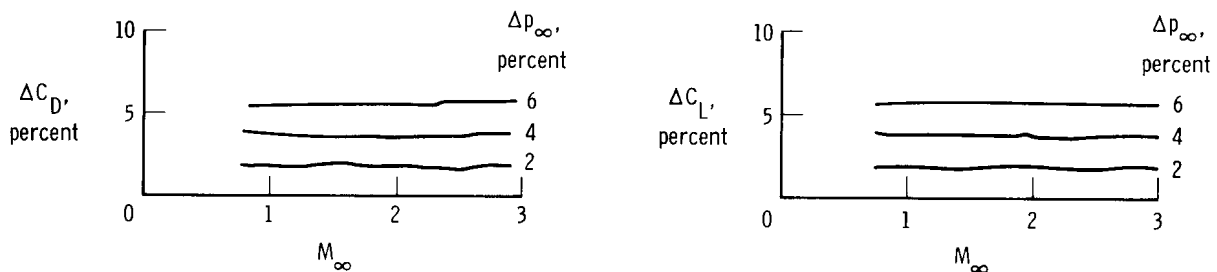


(d) Errors in engine gross thrust. For $\Delta F_g = 6$ percent, $\Delta C_D < 0.1$ percent.

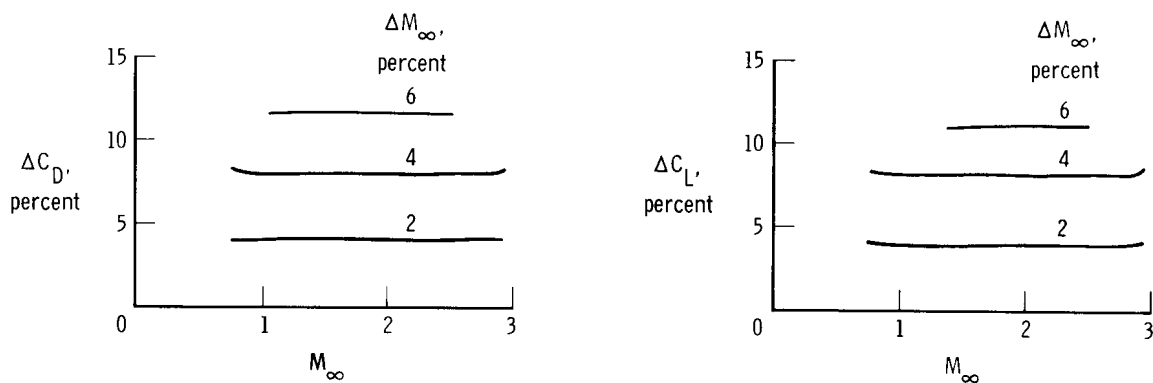
Figure 13. Sensitivity of C_L and C_D to small errors in various parameters. Percentages refer to total airplane lift or drag.



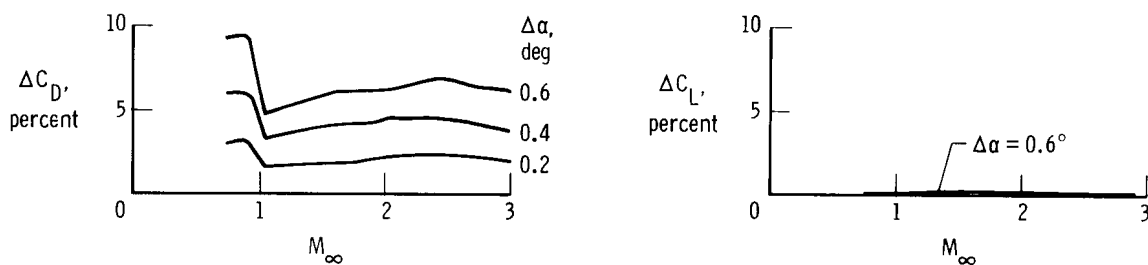
(e) Errors in airplane weight.



(f) Errors in free-stream static pressure.



(g) Errors in free-stream Mach number.



(h) Errors in angle of attack.

Figure 13. Concluded.

The errors in C_L and C_D due to each variable were obtained by combining the information in table 3 and figure 8 with the results shown in figure 13. The errors were added in a root-sum-square calculation to estimate the uncertainty in the lift and drag coefficients. These uncertainties are presented in figure 14 as a function of Mach number. For the XB-70-1 airplane, the uncertainty in C_D is largest at

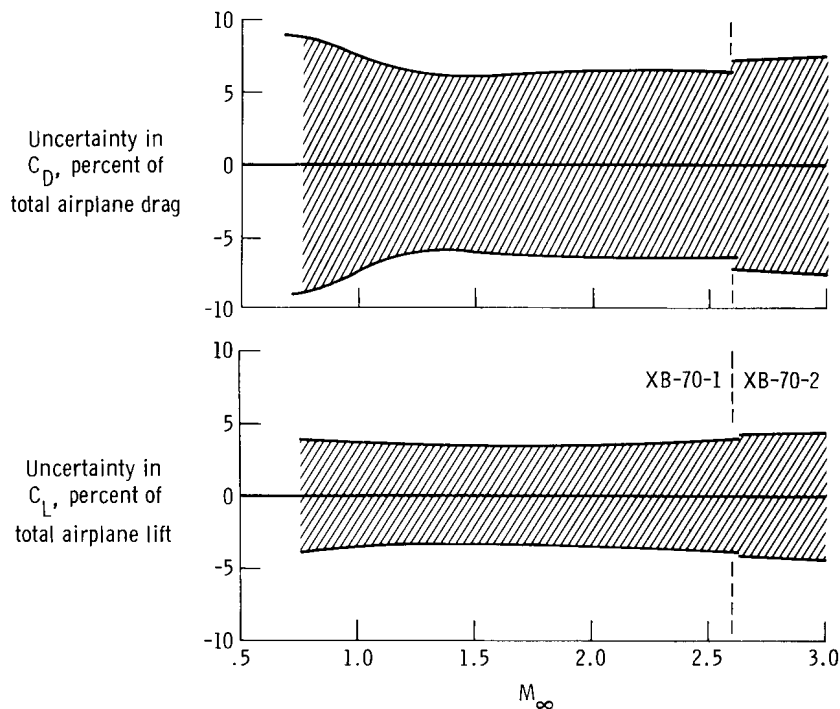


Figure 14. Estimated uncertainty in C_L and C_D from accumulation of errors in lift and drag coefficient variables.

subsonic Mach numbers, where it is approximately ± 9 percent. Figure 13 indicates a large portion of the uncertainty to be due to errors in n_X and α . The uncertainty diminishes to a minimum of ± 6 percent at a Mach number of approximately 1.4. From Mach numbers of 1.8 to 2.5, the error is relatively constant at ± 6.5 percent. The uncertainty in lift coefficient is relatively constant with Mach number at approximately ± 4 percent. The uncertainties in C_L and C_D are larger for the XB-70-2 airplane because the instrumentation for this airplane was less accurate.

The uncertainties shown in figure 14 result from estimates of the errors in the parameters used in the lift and drag equations. The repeatability of the lift and drag measurements, which are presented later, is well within the uncertainty shown in figure 14.

AIRPLANE CONFIGURATION

Airplane performance is sensitive to configuration, so the airplane configurations are reviewed herein before the flight data are presented.

Wingtip Position

Figure 2 shows the nominal operating schedule and limits of the wingtip surface deflections. For the flight data, the actual wingtip positions deviated slightly from nominal. The actual positions are shown in figure 15 for both wingtips.

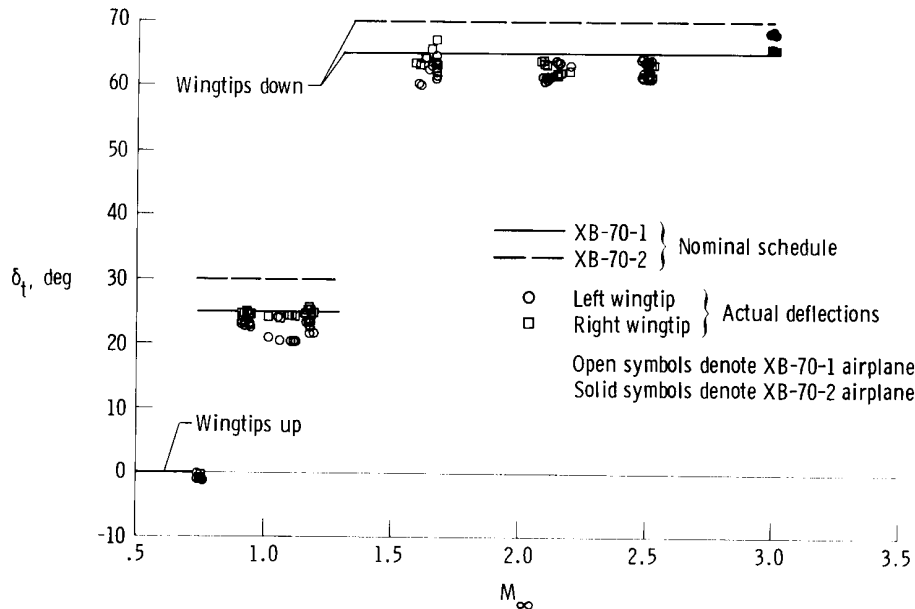


Figure 15. Nominal and actual wingtip positions for flight-measured performance points.

Elevator and Canard Surface Position

Pitch control was obtained by elevator and canard deflections, and it was used to balance out the moments in the airplane longitudinal plane about the center of gravity. The elevator and canard were geared together and were supposed to operate on the schedule shown in figure 16, although there were slight deviations from this schedule in flight (ref. 1).

Under trimmed flight conditions, the elevator and canard positions were scheduled according to many variables. Of these, the location of the center of gravity and load factor n_z , which could be determined in flight, were most significant. Figure 17 shows the center of gravity location for all the flight data. Figure 18 shows the variation of elevator position with Mach number for trimmed flight near $1g$.

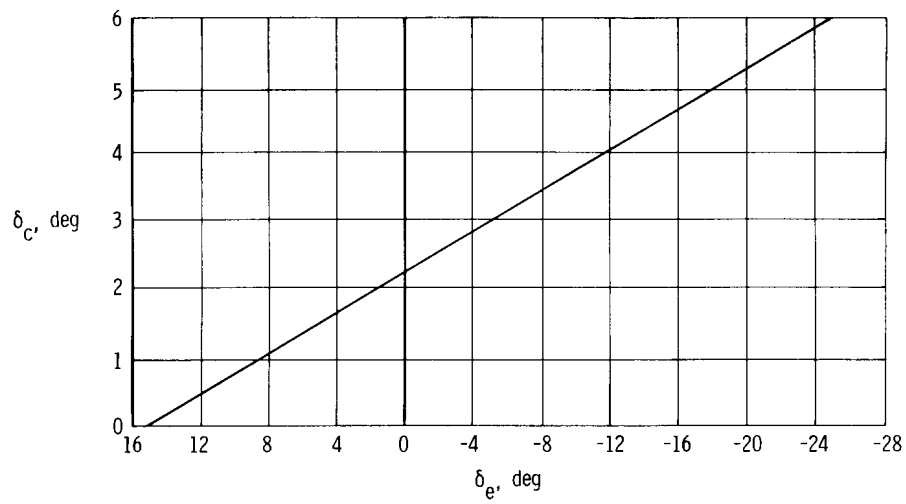


Figure 16. Variation of XB-70-1 canard deflection with elevon deflection. $\delta_c = 2.25^\circ - 0.15\delta_e$.

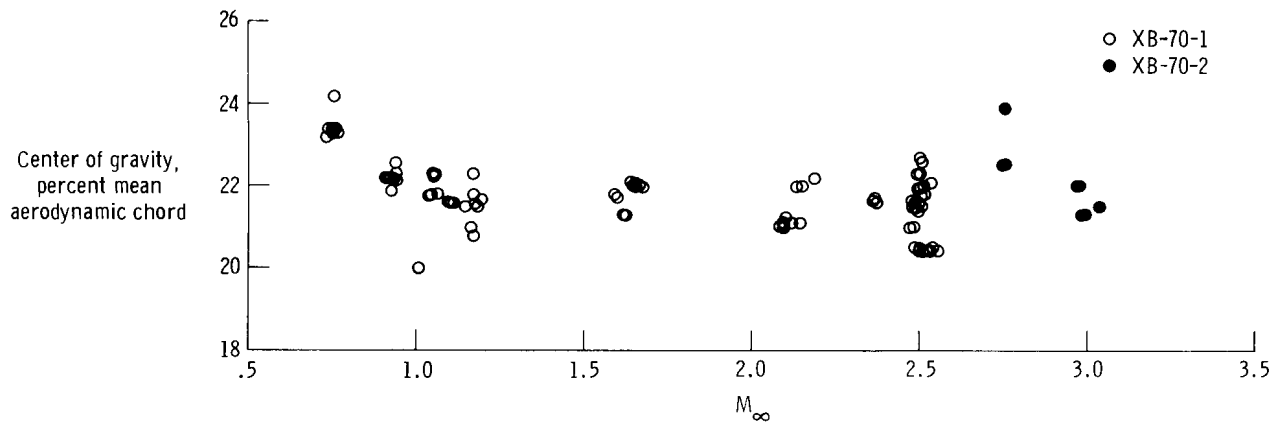


Figure 17. Airplane center of gravity locations.

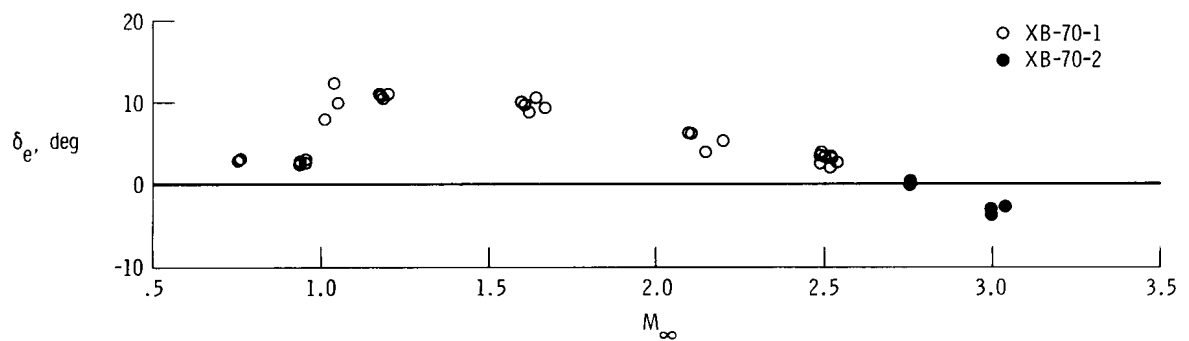


Figure 18. Elevator positions for trimmed flight near 1g.

Aileron and Rudder Position

Aileron and rudder positions, δ_a and δ_r , were near zero for all the flight data. The small deviations from zero that were required to fly the airplane at zero angles of roll and yaw are shown in figures 19 and 20, respectively.

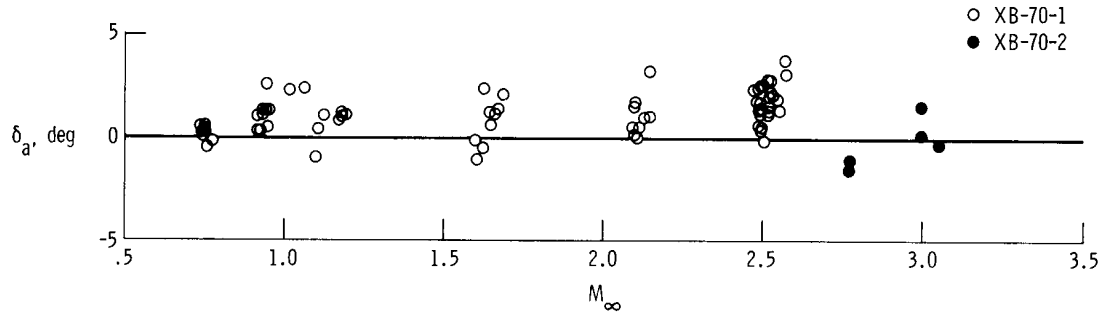


Figure 19. Aileron positions for flight data.

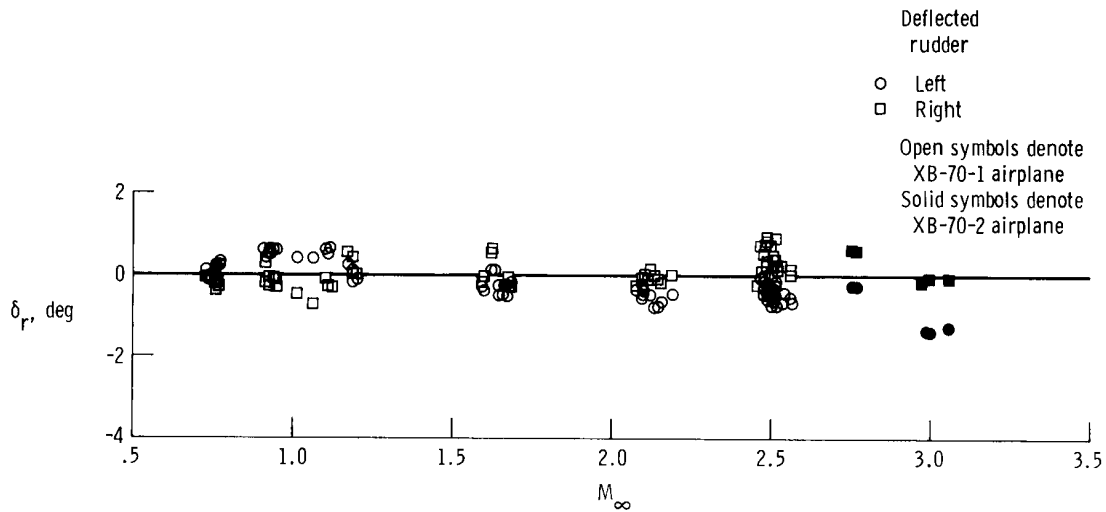


Figure 20. Rudder positions for flight data.

Structural Flexibility

Although the deformation of the airplane's structure was not measured in flight, reference 1 provides analytical predictions of the magnitude of the airplane's structural deformations and the effects of the deformations on aircraft performance for the 14 flight conditions identified in table 4.

Propulsion System

Airplane configuration was also changed by opening the inlet bypass doors and moving the inlet ramps. Only the effects of the bypass doors, which affected C_L , C_D , and pitching moment, were unaccounted for in the airplane performance calculations, however, because the effects of the inlet ramps were accounted for in the calculation of F_{nt} . Figure 21 indicates the range of the measured in-flight door deflections for all flight conditions and for all 12 bypass doors (figs. 1 and 5).

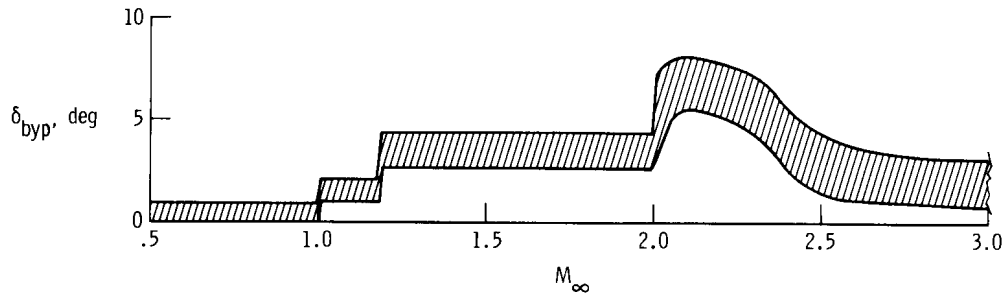


Figure 21. Variation of inlet bypass door deflection with Mach number. Range indicates variation in all doors and during all flights.

Miscellaneous Configuration Changes

Other slight configuration changes were made during or between flights. For example, the nose ramp in front of the cockpit was designed to be in the up position for supersonic flight, but it was usually kept down during the research flights for increased visibility. Other configuration changes involved such research hardware as probes, boundary layer rakes, and vanes, which were periodically put on and taken off the airplane. The effects of these changes and others on the airplane's performance are discussed in more detail in reference 1.

RESULTS AND DISCUSSION

Performance Measurements

Lift, drag, and angle of attack measurements were made in flight at 99 flight conditions. The measurements were obtained at Mach numbers from 0.72 to 3.07 and altitudes from approximately 7620 meters (25,000 feet) to 21,340 meters (70,000 feet).

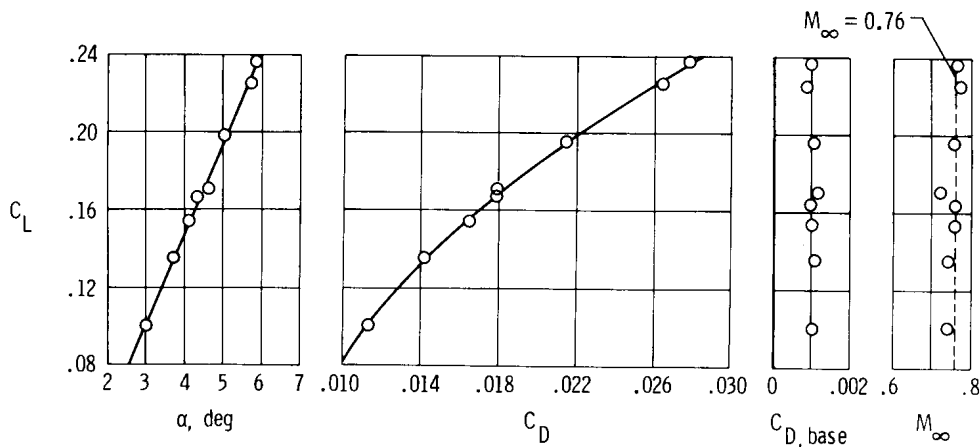
The data were acquired about distinct test Mach numbers. Large variations in C_L and C_D were made deliberately at some of these Mach numbers by using roller coaster maneuvers.

Figure 22 presents the flight values of α , C_D , and $C_{D,base}$ as a function of lift coefficient, C_L . The base drag coefficient, $C_{D,base}$, which was a significant component of the airplane drag at certain Mach numbers, was measured as described in reference 12. The base drag component, which is included in C_D , varied with Mach number and, at transonic Mach numbers, with engine power setting. As shown in figure 22, the variations in Mach number for the various values of C_L about the nominal test Mach numbers are small.

At the Mach numbers for which data were sufficient and variations in C_L were large, curves were faired through the data for α and C_D . A least-squares-fit procedure was used to fair the data. A linear fit was used for α and a parabolic fit was used for C_D .

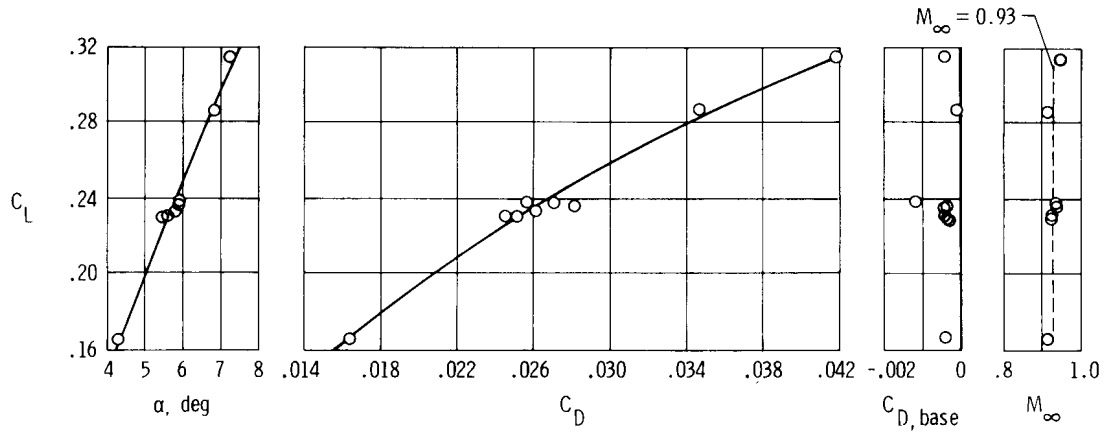
The data for the two airplanes were obtained at different Mach number ranges; for the XB-70-1 airplane, the Mach number range was from 0.72 to 2.57, and for the XB-70-2 airplane, the Mach number range was from 2.76 to 3.07.

Subsonic performance.—Figures 22(a) and 22(b) show the performance of the XB-70-1 airplane at subsonic Mach numbers ($M_\infty \approx 0.76$ and 0.93). The base drag coefficient is approximately 0.0010 for a Mach number of 0.76, and it becomes negative (approximately -0.0004) at Mach 0.93. In the Mach 0.93 data, there was a change of nearly 0.0008 in the base drag coefficient at a lift coefficient of approximately 0.23 due to engine power changes.



(a) $M_\infty \approx 0.76$, $\delta_t \approx 0^\circ$, XB-70-1 airplane.

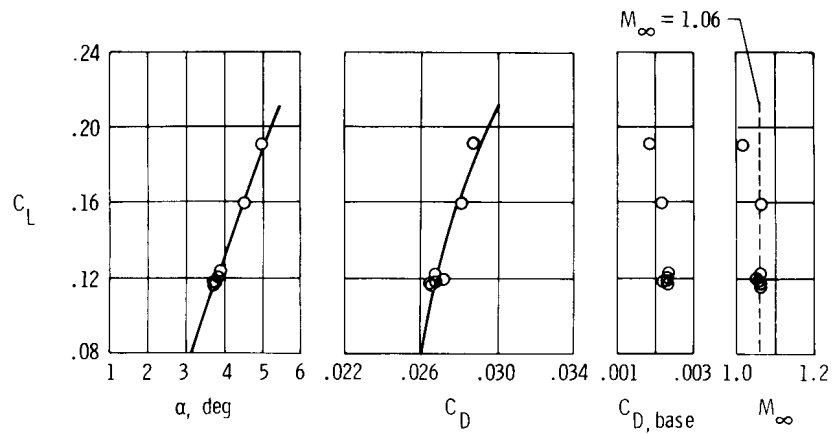
Figure 22. Measured trimmed flight performance.



(b) $M_\infty \approx 0.93$, $\delta_t \approx 25^\circ$, XB-70-1 airplane.

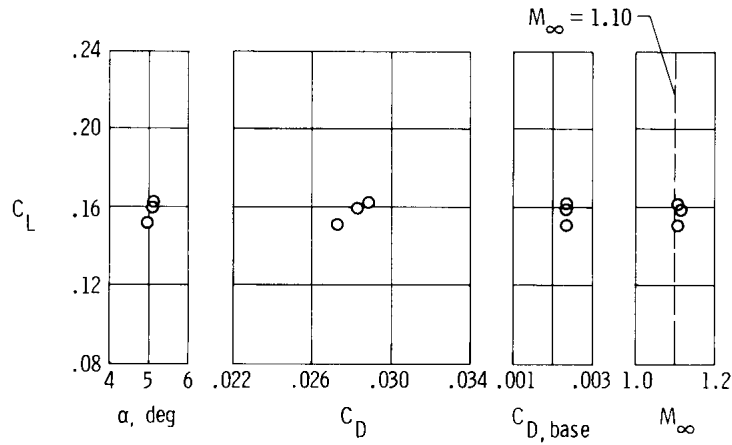
Figure 22. Continued.

Transonic performance.—Figures 22(c) to 22(e) show the performance of the XB-70-1 airplane at transonic Mach numbers ($M_\infty \approx 1.06$ to 1.18). A comparison of figures 22(b) and 22(c) shows that the drag coefficient for a lift coefficient near 0.16 rises from approximately 0.016 at Mach 0.93 to approximately 0.028 at Mach 1.06.

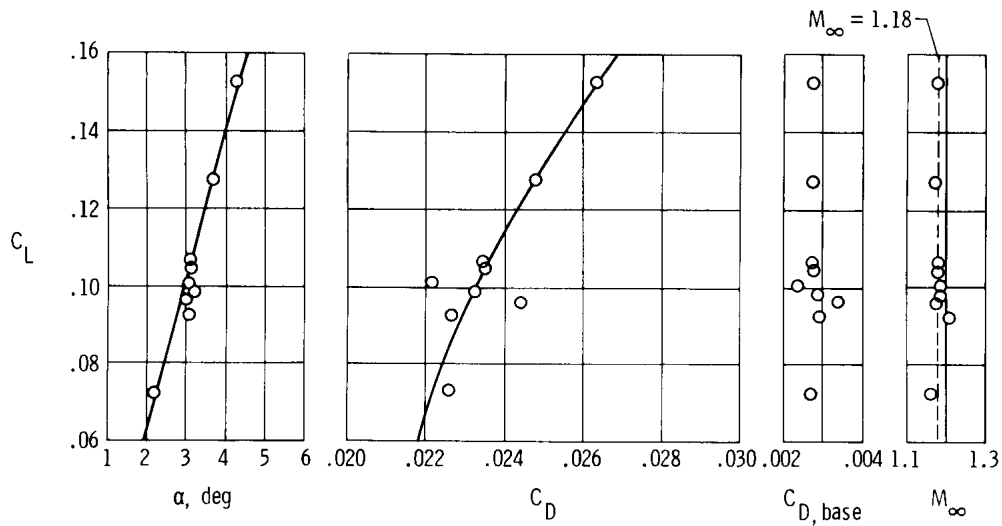


(c) $M_\infty \approx 1.06$, $\delta_t \approx 25^\circ$, XB-70-1 airplane.

Figure 22. Continued.



(d) $M_\infty \approx 1.10$, $\delta_t \approx 25^\circ$, XB-70-1 airplane.



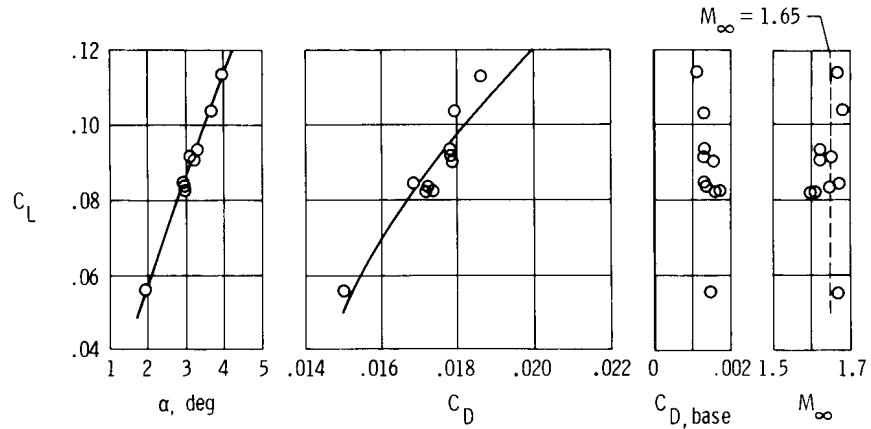
(e) $M_\infty \approx 1.18$, $\delta_t \approx 25^\circ$, XB-70-1 airplane.

Figure 22. Continued.

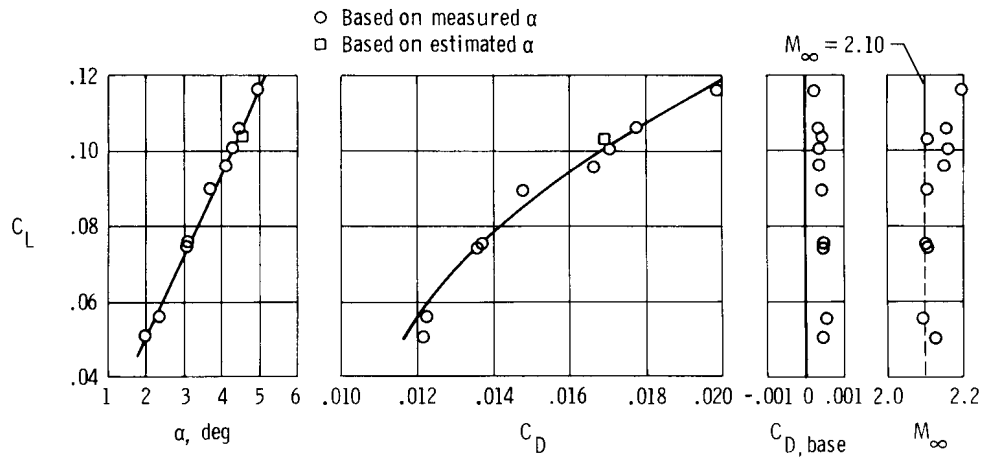
Figure 22(e), for $M_\infty \approx 1.18$, shows that there is a significant amount of scatter in the data for a lift coefficient of approximately 0.10, which were acquired in 1g flight. Changes in base drag account for some of this scatter; base drag is at its maximum value at this Mach number, where it constitutes approximately 12 percent of the airplane drag. The rest of the scatter is believed to be due to differences in airplane drag due to engine power.

Wave and afterbody drag are dominant at transonic Mach numbers, and therefore drag coefficient does not change much with lift coefficient, especially at Mach 1.06.

Supersonic performance.—Figures 22(f) to 22(i) show the supersonic performance of the XB-70-1 airplane. Drag polars were obtained at Mach numbers of approximately 1.65, 2.10, and 2.50.

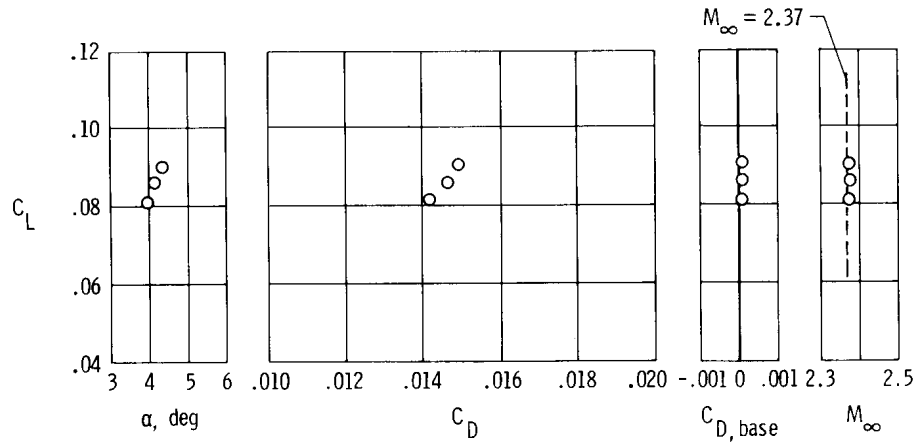


(f) $M_\infty \approx 1.65$, $\delta_t \approx 65^\circ$, XB-70-1 airplane.

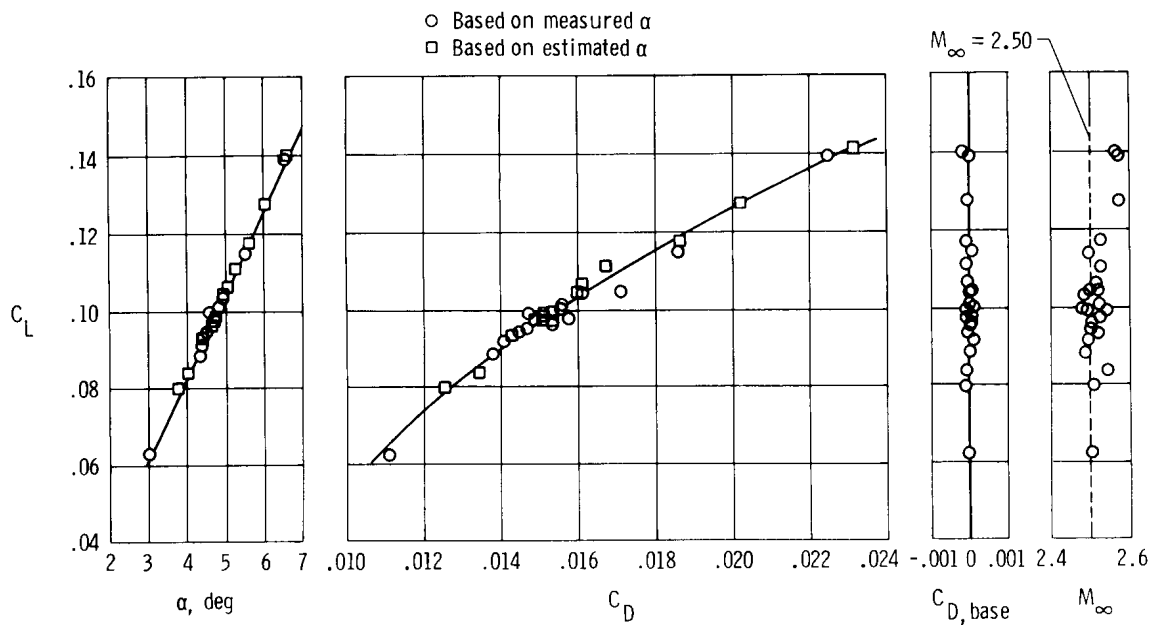


(g) $M_\infty \approx 2.10$, $\delta_t \approx 65^\circ$, XB-70-1 airplane.

Figure 22. Continued.



(h) $M_\infty \approx 2.37$, $\delta_t \approx 65^\circ$, XB-70-1 airplane.

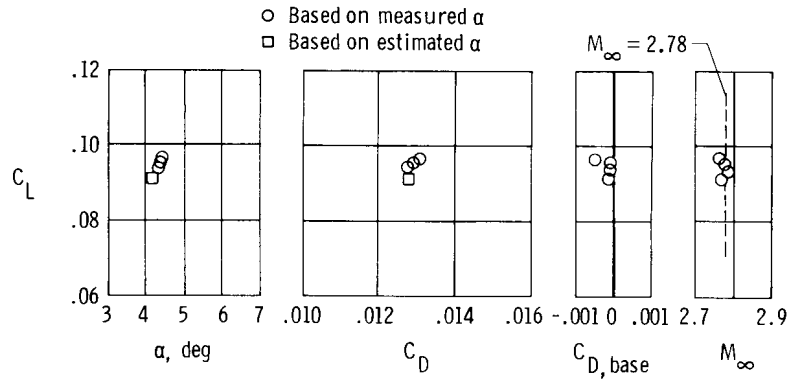


(i) $M_\infty \approx 2.50$, $\delta_t \approx 65^\circ$, XB-70-1 airplane.

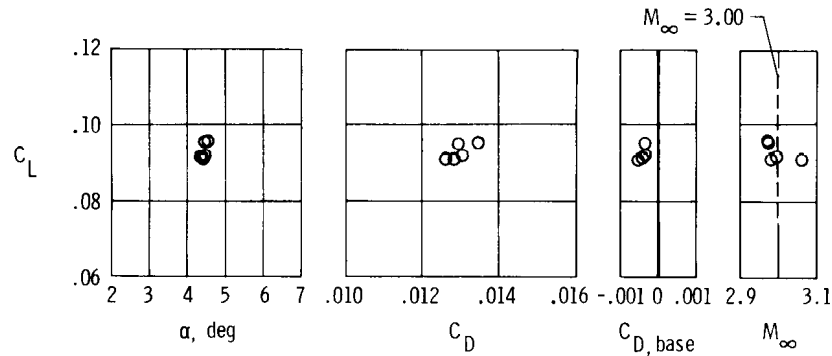
Figure 22. Continued.

Estimates of angle of attack had to be made for several of the data in figures 22(g), 22(i), and 22(j) because angle of attack measurements were not available. The estimates were made by fairing the C_L versus α data obtained for the same Mach number from other flights. Values of angle of attack were taken from these fairings according to lift coefficient. Because angle of attack was required for calculating lift coefficient, an iteration process was used to obtain the final estimate of angle of attack.

High supersonic performance.—Figures 22(j) and 22(k) show the high supersonic performance of the XB-70-2 airplane ($M_\infty \approx 2.78$ and 3.00). Only a few



(j) $M_\infty \approx 2.78$, $\delta_t \approx 70^\circ$, XB-70-2 airplane.

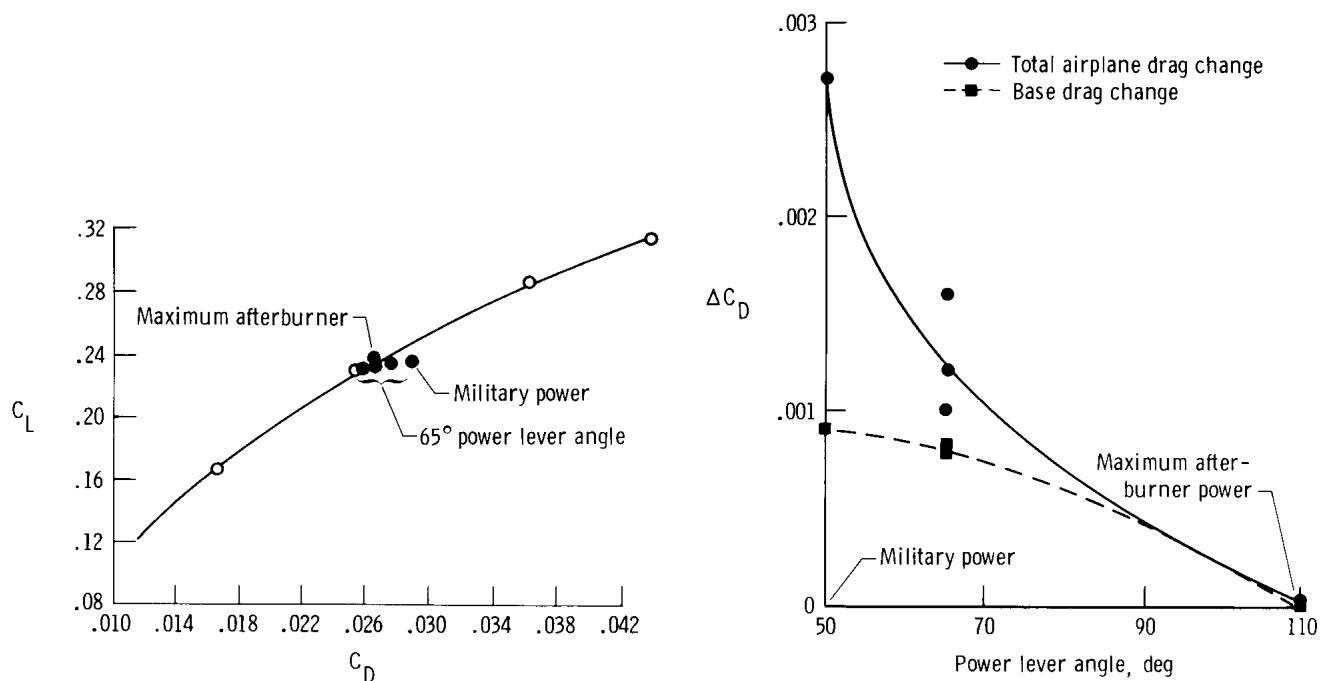


(k) $M_\infty \approx 3.00$, $\delta_t \approx 70^\circ$, XB-70-2 airplane.

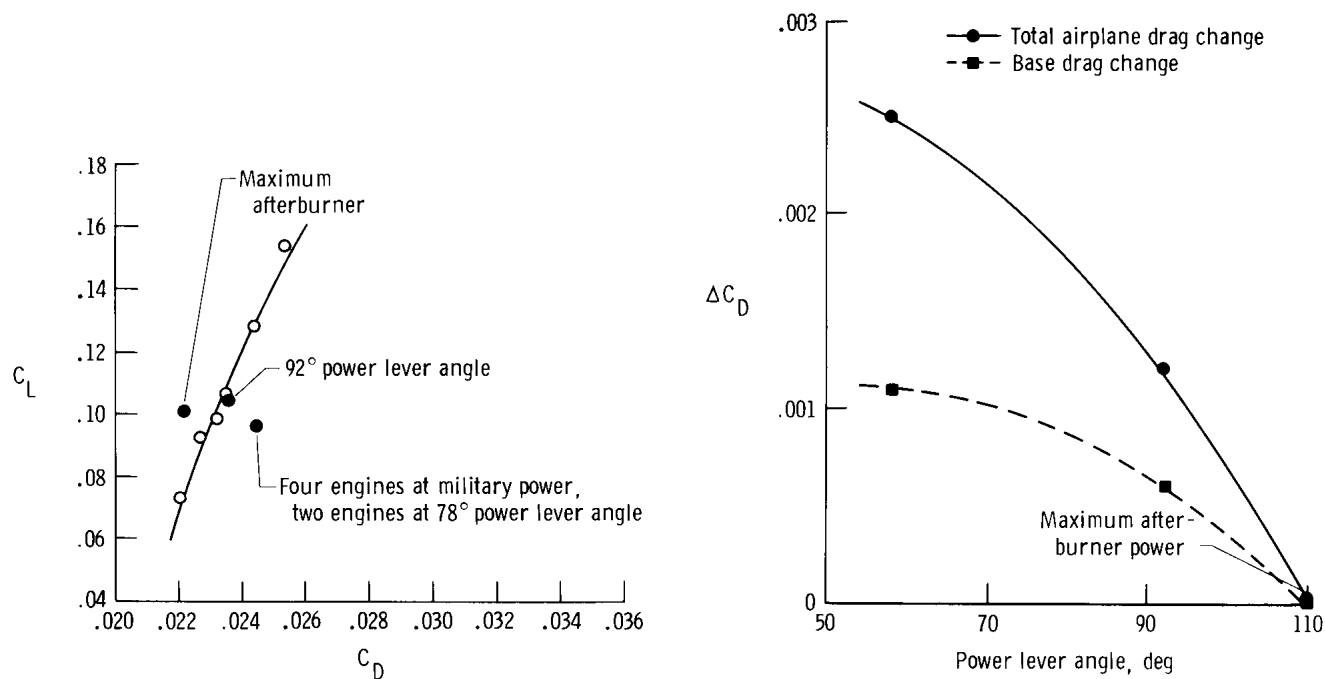
Figure 22. Concluded.

performance data of good quality were obtained for this airplane, and then only at high Mach numbers. No attempt was made to generate drag polars because these data were obtained early in the airplane's evaluation, when maneuvering was restricted.

Effects of engine power.—Scatter in airplane drag due to differences in engine power was noted in the transonic Mach number region. This scatter is apparent in figure 23 in the data for a lift coefficient near 0.23 for a Mach number of approximately 0.93 and in the data for a lift coefficient of 0.10 for a Mach number of approximately 1.18. The difference between the drag measured at maximum afterburner power and at other power lever angle settings is also shown in the figure. The changes in base drag, which were measured in flight independent of F_{nt} , are also shown. Part of the change in overall drag resulted directly from the change in base drag; the rest of the change is believed to be due to changes in boattail drag, although this was not demonstrated. Uncertainty in the calculation of F_{nt} may also have contributed to the change.



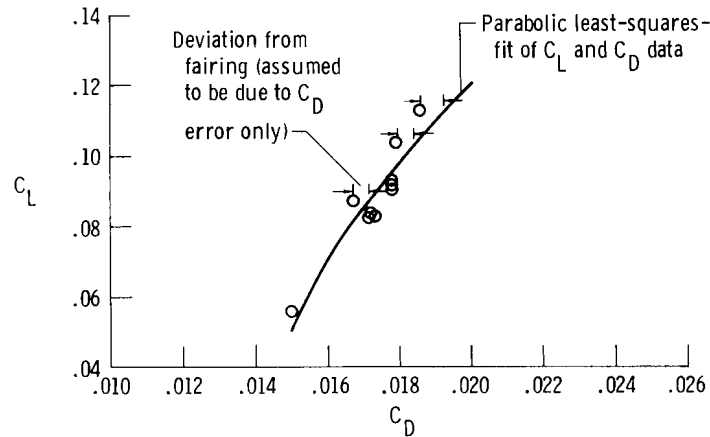
(a) $M_\infty \approx 0.93$. Solid symbols indicate data used to establish engine power effects.



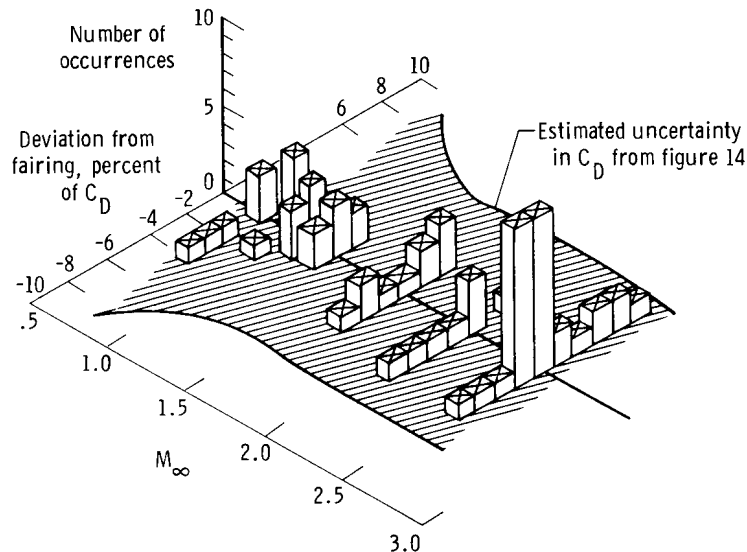
(b) $M_\infty \approx 1.18$. Solid symbols indicate data used to establish engine power effects.

Figure 23. Changes in drag with engine power lever angle (averaged for six engines). Drag increments referenced to maximum afterburner power condition and corrected for lift effects.

Repeatability of lift-drag data.—The repeatability of the lift and drag data was tested by comparing the scatter about the fairings through the C_L and C_D data with the estimated uncertainty in C_D (fig. 14). Only the drag coefficient was examined, and for practical purposes it was assumed that the scatter about the fairing resulted from errors in C_D only (fig. 24(a)). Figure 24(b) shows that the scatter about the fairing is well within the uncertainty band presented in figure 14. Although this



(a) Typical drag polar data showing deviation used to determine repeatability of drag data. $M_\infty \approx 1.65$.



(b) Drag data scatter about drag polar fairings with Mach number.

Figure 24. Summary of repeatability of lift and drag data. Corrected for differences in engine power and base drag.

approach is not adequate proof that the accuracy of the data is much greater than was estimated, because bias errors are not accounted for, it does indicate that the repeatability, or precision, of the data is better than indicated by figure 14. This concept is supported by the fact that the deviations in the data presented in figure 24(b) include errors in both C_L and C_D , and not errors in C_D only, and by the fact that some of the deviations may have been due to the configuration changes discussed earlier. The data points which show the effects of differences in engine power on drag, which are shown in figure 23, were not included, and the data were also corrected for differences in base drag.

Base drag.—The variation of base drag with Mach number is shown in figure 25. There is a large change in base drag coefficient (approximately 0.0025) at Mach 1.00, and the base drag peaks out at a Mach number near 1.20. The base drag is negative at Mach numbers near 0.90 and at those above 2.50.

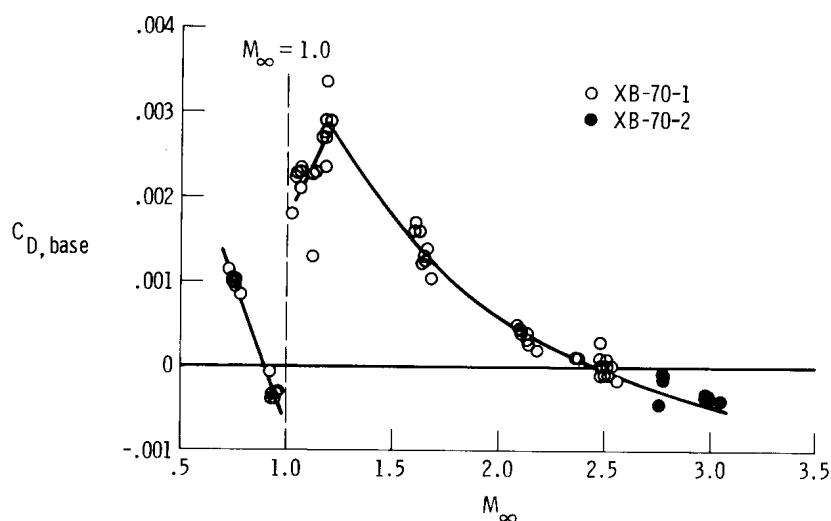


Figure 25. Summary of base drag coefficients measured in flight.

Drag Polar Analysis and Summary

The drag polars obtained over the Mach number range from approximately 0.76 to 2.50 were also analyzed to provide information about the aircraft's lift-induced drag, $\frac{\Delta C_D}{\Delta C_L^2}$; minimum drag, C_{D0} ; and maximum lift-to-drag ratio, $(L/D)_{max}$.

The variation of the trimmed airplane drag with Mach number at constant lift coefficients was also determined.

Lift-induced and minimum drag.—The drag polars, which were least-square-type parabolic fits of the data, were plotted as straight lines in plots of C_L^2 versus

C_D as shown in figure 26. The inverse of the slope of the lines, $\frac{\Delta C_D}{\Delta C_L^2}$, which represents the lift-induced drag of the trimmed airplane, is plotted as a function of Mach number in figure 27 for the airplane at three wingtip deflections.

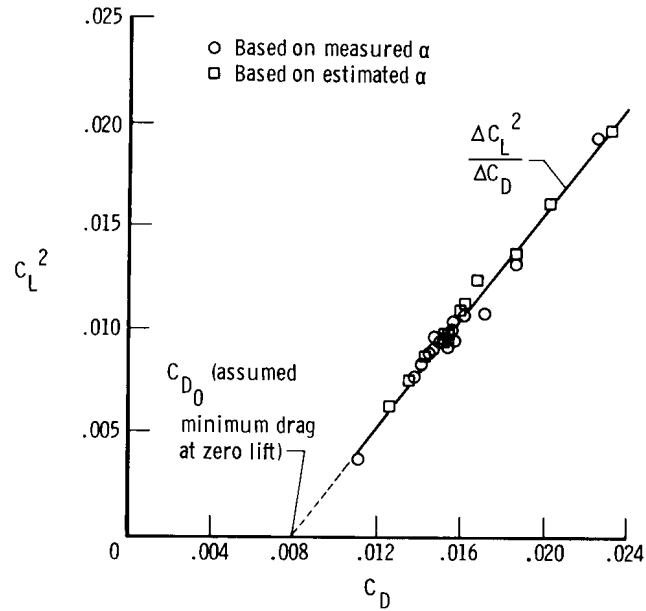


Figure 26. Typical plot of C_L^2 versus C_D illustrating the slope $\frac{\Delta C_L^2}{\Delta C_D}$ and the minimum drag coefficient, C_{D0} , of the faired curve. $M_\infty \approx 2.50$.

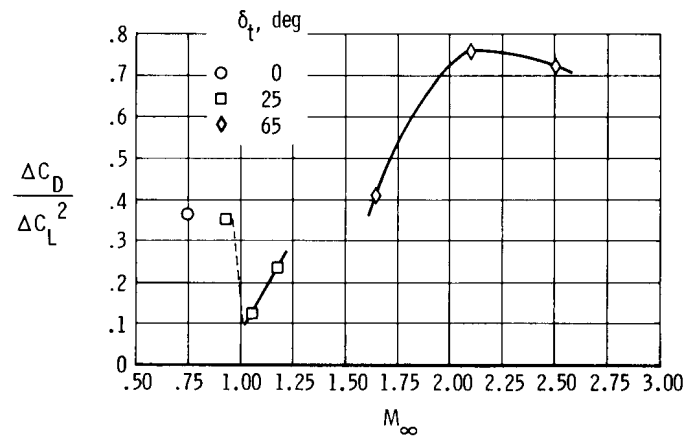


Figure 27. Variation of $\frac{\Delta C_D}{\Delta C_L^2}$ with Mach number for trimmed conditions.

If it is assumed that the drag polars are parabolic and that drag is at a minimum at zero lift, values of minimum drag, C_{D_0} , can be obtained by extrapolating the drag polar as shown in figure 26. These minimum drag values are plotted as a function of Mach number in figure 28 for the three wingtip deflections. Although the

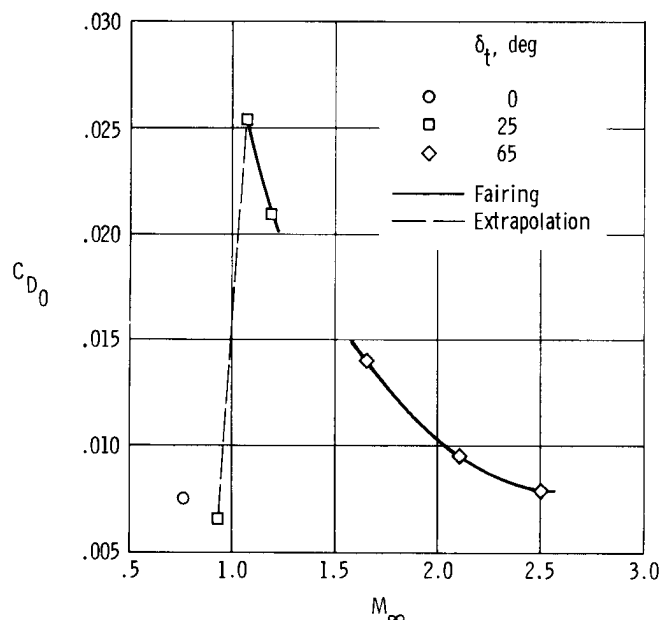
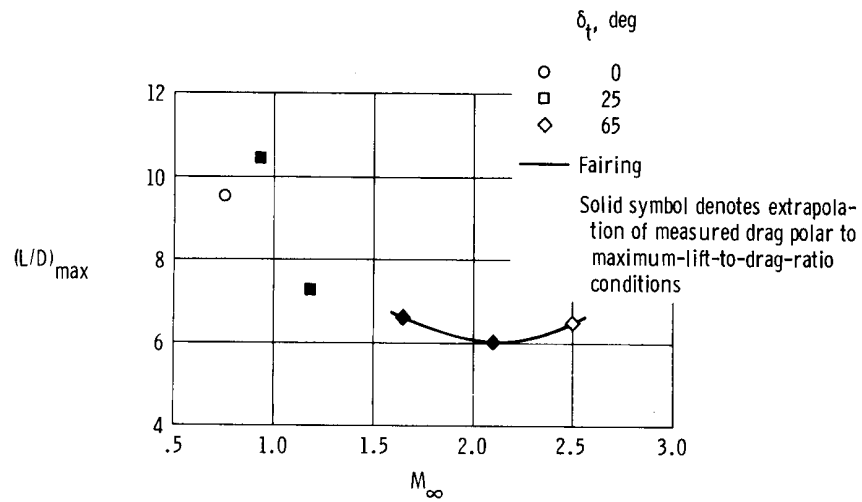


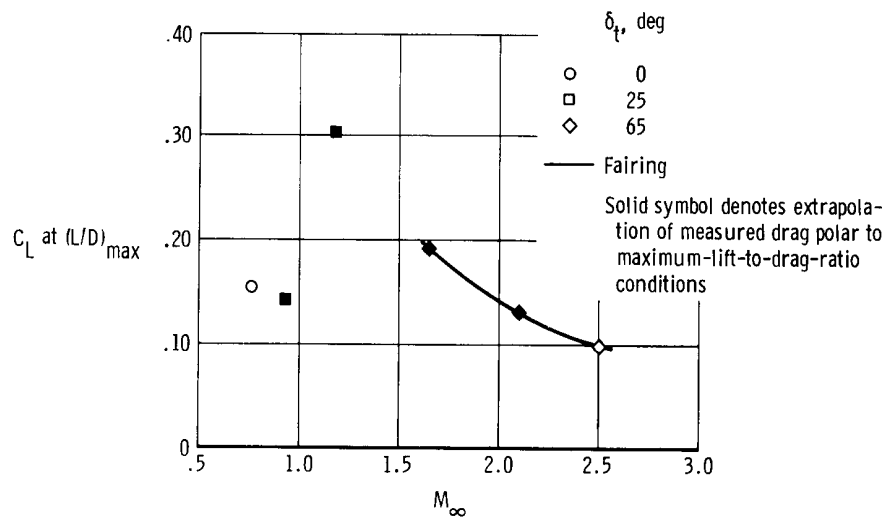
Figure 28. Minimum drag, C_{D_0} , as a function of Mach number for trimmed conditions. Obtained by extrapolating linear curves as shown in figure 26 to zero lift.

assumption that the polars are parabolic seems to be valid, at least for the data available, the assumption that drag is at a minimum at zero lift is open to question because it was not possible to verify the assumption with flight data.

Maximum lift-to-drag ratio.—Maximum lift-to-drag ratios, $(L/D)_{max}$, were also obtained from the drag polars, and figure 29 presents these ratios as a function of Mach number for the three wingtip deflections. Included in the figure are the lift coefficients required to generate $(L/D)_{max}$. No value was obtained for $(L/D)_{max}$ for Mach 1.06 because the lift coefficient required to generate the maximum lift-to-drag ratio was beyond the flight profiles flown at this Mach number.



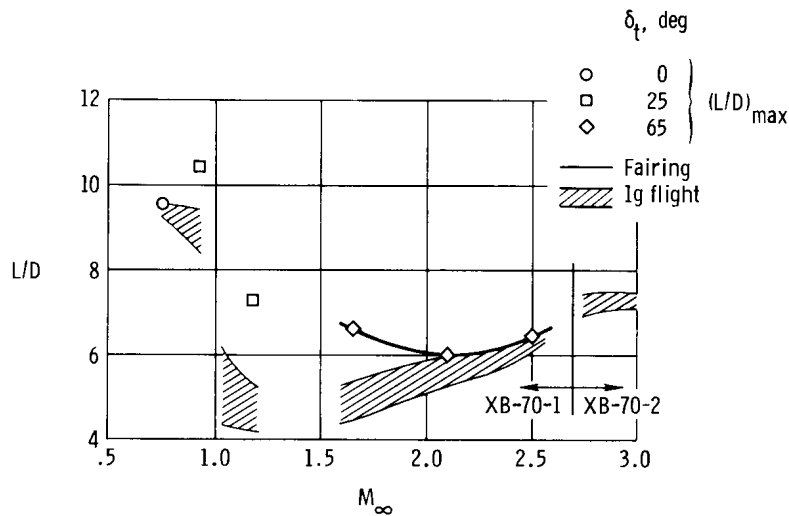
(a) Maximum lift-to-drag ratios.



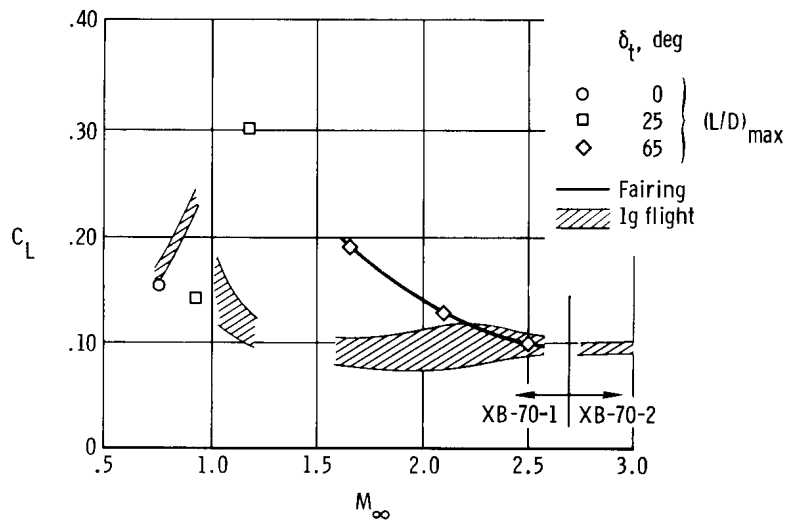
(b) Lift coefficients at $(L/D)_{max}$.

Figure 29. Maximum lift-to-drag ratio and lift coefficient required to generate maximum lift-to-drag ratios as a function of Mach number under trimmed conditions.

In figure 30, the $(L/D)_{max}$ results shown in figure 29 are compared with the lift-to-drag ratios flown under 1g flight conditions near the climb profile in figure 9. The lift coefficients for the corresponding conditions are also shown. The airplane normally flies at or near $(L/D)_{max}$ at low subsonic and high supersonic speeds only, where the measured trimmed $(L/D)_{max}$ values are approximately 9.5 and 6.5, respectively. At transonic and low supersonic speeds, the airplane flies at much lower lift coefficients than those required to generate $(L/D)_{max}$. The lift-to-drag ratios for the XB-70-2 airplane were obtained with wingtips deflected approximately 68° .



(a) Lift-to-drag ratios.



(b) Lift coefficients.

Figure 30. Comparison between conditions for $(L/D)_{max}$ and lift-to-drag ratios obtained in 1g flight as a function of Mach number.

Lift and drag summary.—Figure 31 summarizes the trimmed lift and drag characteristics of the XB-70 airplane as indicated by the drag polars. The variation of drag

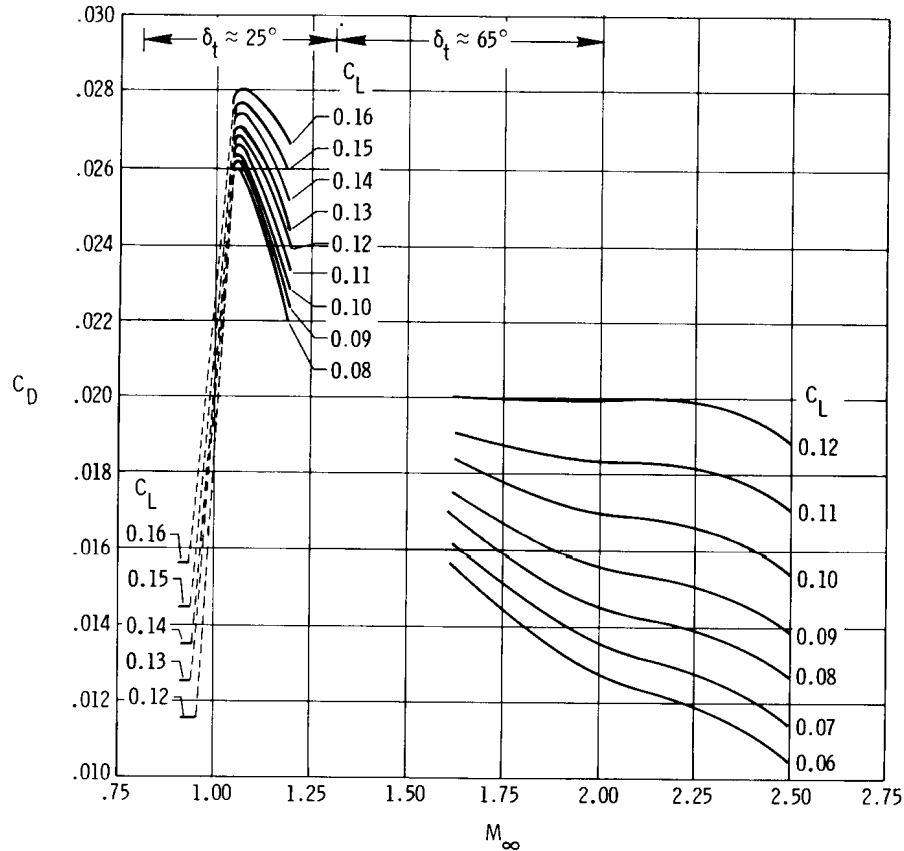
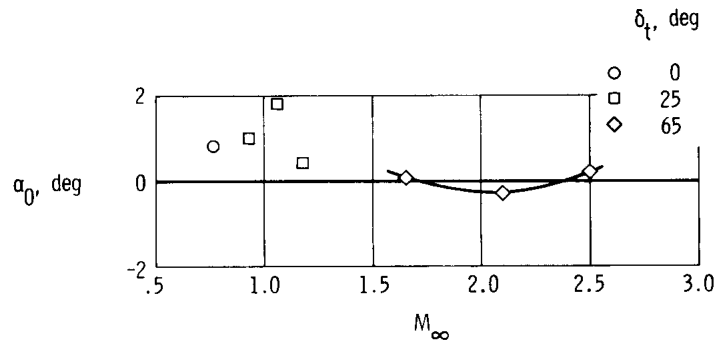


Figure 31. Summary of trimmed drag coefficient variation with Mach number at constant lift coefficients for nominal wingtip positions of 25° and 65°. XB-70-1 airplane.

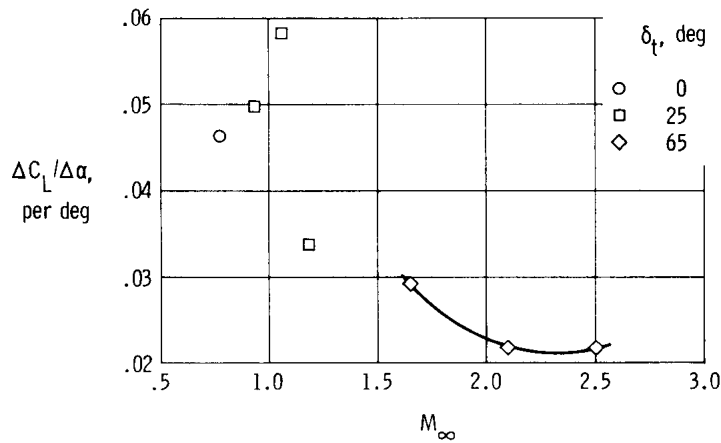
coefficient with Mach number is shown for constant lift coefficients for nominal wingtip deflection positions of approximately 25° and 65°. Figure 31 illustrates the magnitude of the transonic drag rise; incremental increases in drag at constant lift coefficients were from 80 percent to 130 percent of the subsonic values.

Angle of Attack Summary

The characteristics of the variation of angle of attack with lift coefficient were obtained from lift-curve slopes and the values of angle of attack at zero lift. These characteristics were obtained by fairing the measured lift coefficient and angle of attack data with straight lines. Figure 32 summarizes these characteristics. Figure 32(a) shows the variation of angle of attack at zero lift, α_0 , with Mach number, and figure 32(b) shows the variation of the lift-curve slope, $\Delta C_L / \Delta \alpha$, with



(a) α_0 .



(b) $\Delta C_L / \Delta \alpha$.

Figure 32. Variation of α_0 and $\Delta C_L / \Delta \alpha$ with Mach number.
Trimmed flight, XB-70-1 airplane.

Mach number. Values for α_0 were obtained by extrapolating the linear curves to a zero lift coefficient.

CONCLUDING REMARKS

The lift and drag characteristics of two XB-70 airplanes were measured in flight over a Mach number range from 0.72 to 3.07 at altitudes from approximately 7620 meters (25,000 feet) to 21,340 meters (70,000 feet). These flights provided a set of performance data for a large, flexible airplane with a design cruise Mach number of 3 in trimmed flight.

Sufficient measurements were made between Mach numbers of approximately 0.76 and 2.50 to establish the variation of lift and angle of attack and drag at several Mach numbers, including transonic Mach numbers. Performance characteristics were defined from these variations in lift, including lift-induced drag, drag at zero lift, maximum lift-to-drag ratio, the lift-curve slope with angle of attack, and the angle of attack at zero lift.

Other measurements provided information about the variation in base drag with Mach number, the changes in airplane drag with engine power changes at transonic speeds, and the magnitude of the drag components charged to the propulsion system.

The following results are representative of the XB-70-1 airplane:

The maximum trimmed lift-to-drag ratio for near 1g flight at a Mach number near 0.93 was approximately 9.5. It was near 6.5 for Mach numbers near 2.5.

The base drag is at the maximum value near a Mach number of 1.2, where it constitutes approximately 12 percent of the total airplane drag.

A large transonic drag rise was observed for this airplane. At constant lift coefficients, incremental increases in drag as high as 130 percent of the subsonic value were noted.

*Dryden Flight Research Center
National Aeronautics and Space Administration
Edwards, Calif., April 27, 1976*

APPENDIX A.—AIRPLANE NET PROPULSIVE THRUST CALCULATION

Airplane net propulsive thrust, F_{nt} , is the algebraic sum of the thrust and drag forces associated with the inlet mass flow entering and exiting the propulsion system. It is determined from engine net thrust and inlet drag as shown in the following expression:

$$F_{nt} = F_n - D_{inlet}$$

where F_n is the engine net thrust and D_{inlet} is the inlet drag due to the propulsion system (fig. 10). The following discussion describes the methods used to obtain F_n and D_{inlet} from flight data.

ENGINE NET THRUST

Engine net thrust is defined as the algebraic sum of the engine gross thrust, F_g , and engine ram drag, F_r , as follows:

$$F_n = F_g - F_r$$

The method used to calculate engine net thrust, which is called the gas generator method, is described in references 3, 9, and 10.

INLET DRAG

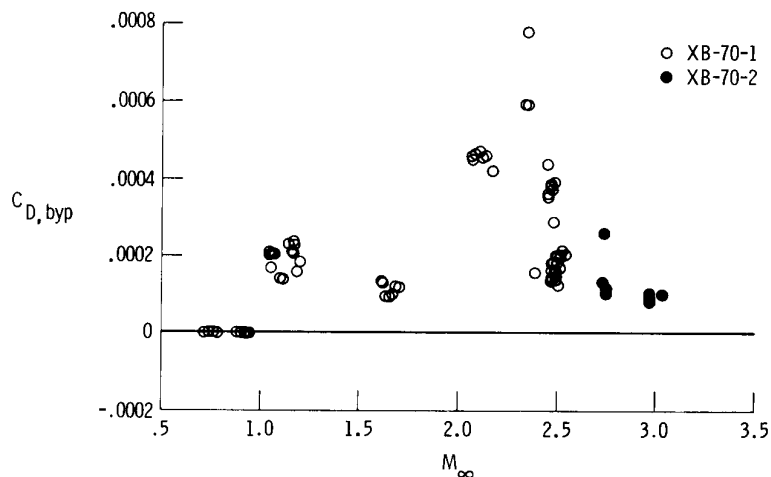
The components of inlet drag are due to the airflows related to the bypass and boundary layer bleed systems. The drag due to these components is the difference between the momentum and pressure of the airflow in the free stream and at the point where it exits the propulsion system. The equation used to calculate the drag due to a component y is as follows:

$$D_y = \dot{m}_y V_\infty - \left[\dot{m}_y V_{y,exit} + A_{y,exit} (p_\infty - p_{y,exit}) \right] \cos \phi_y$$

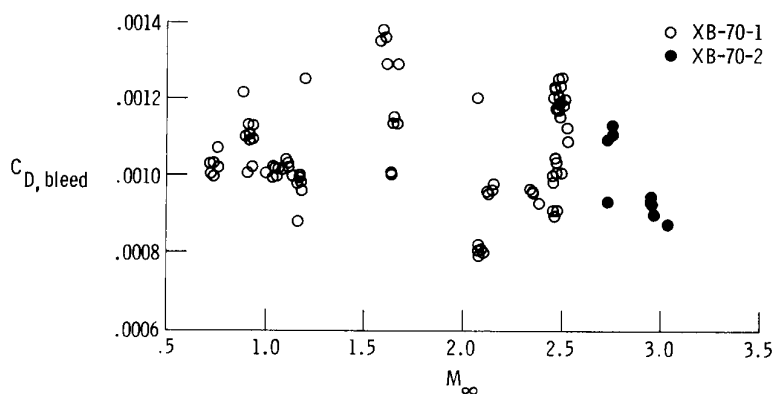
A conventional compressible fluid flow analysis (refs. 13 and 14) was used to determine the mass flow, \dot{m} ; the exit airflow velocity, V ; static pressure, p ; and effective flow area, A , for each of the drag components. The types of measurements used in these calculations are listed in table 2 along with sensor accuracies and ranges. It was assumed that all inlet component airflows, unless otherwise specified, discharged to the free-stream static pressure, p_∞ . The total temperatures of these airflows were T_{t_∞} . The flow discharge angle, ϕ , was used to resolve the component forces along the airplane's flightpath.

APPENDIX A.—Continued

Figure 33 summarizes the inlet drag components measured in flight. Figure 33(a) shows the drag due to the inlet bypass system and figure 33(b) the drag due to the inlet boundary layer bleed system. The cross-hatched regions in figure 11 are derived from these data.



(a) Drag coefficients for inlet bypass system.



(b) Drag coefficients for inlet boundary layer bleed system.

Figure 33. Inlet drag components measured in flight.

The calculations used to determine these drag components are described below.

Inlet Bypass Door Drag

Inlet air passed out of each inlet through six doors. The doors were in pairs on top of the airplane (figs. 1 and 5). To increase the exit velocity of the bypass flow

at the doors, the doors were designed to form a convergent nozzle at large door openings and a convergent-divergent nozzle at small door openings.

The procedure for calculating the exit airflow properties \dot{m}_{byp} , V_{byp} , and p_{byp} and the effective flow area A_{byp} depended on whether the doors created a convergent-divergent nozzle or a convergent one and on whether the flow was subsonic, sonic, or supersonic at the exit plane.

The effective flow areas and throat-to-exit area ratios of the doors were determined from the bypass door deflection angle, δ_{byp} , along with door calibrations and coefficients. The variables in the drag calculation for the doors were obtained from the door geometry, the measured total pressure of the bypass airflow, free-stream static pressure, and free-stream total temperature.

Boundary Layer Bleed System Drag

To improve the efficiency and stability of the operation of the inlet, a boundary layer bleed system was provided in the vicinity of the inlet throat. Boundary layer air was removed from the inlet at various locations near the inlet throat. Part of the air was removed by a ram scoop, called an inlet diverter, which channeled air through a rectangular passage in the wing and dumped it overboard through the exit shown in figures 1 and 5. The rest of the bleed air was removed through porous bleed panels, which were in four zones (fig. 34). These zones were tailored to the

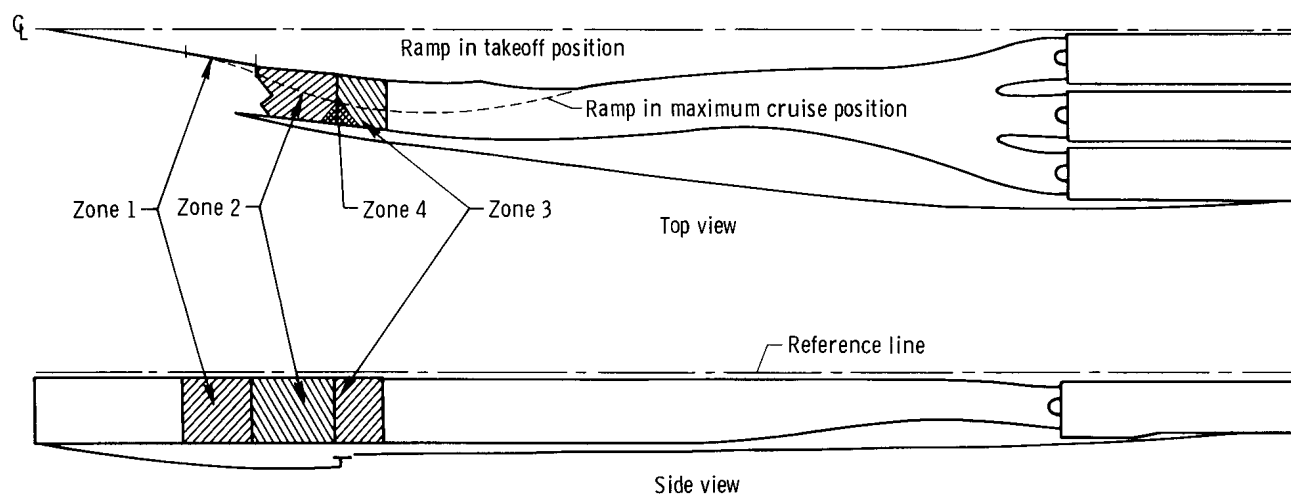


Figure 34. Inlet boundary layer bleed zones.

pressure levels that existed in the inlet near the throat when the inlet was operating in the mixed-compression mode. The zones were separated into compartments to eliminate crossflow. The bleed air from each zone was dumped overboard at a different location on the airplane.

APPENDIX A.—Concluded

The drag due to the inlet diverter and each bleed zone was determined separately and for the left inlet only; it was assumed that the drag in the right inlet was the same as in the left. The drag calculation for each bleed component is described below.

Inlet diverter drag.—The boundary layer air along the top surface of the inlet was removed by the inlet diverter. The drag due to this system was determined from pressures measured in the diverter's rectangular passage and the geometric characteristics of the passage. Total pressures were sensed with two four-probe rakes. Static pressures were sensed with four static pressure ports in the plane of the total pressure measurement.

Bleed zones 1 and 2.—In zone 1, the first porous panel section passed by incoming air (fig. 34), only the inlet ramp wall on the fuselage side was porous and used to bleed air. Zone 2 was adjacent to zone 1 on the downstream side, but three of the four walls of the inlet were porous. The top surface of the inlet was not bled in this section, since the boundary layer on this surface had been removed by the inlet diverter.

The air from these two zones was dumped overboard through a bleed dump fairing underneath the inlet (figs. 4 and 5). Total and static pressures sensed at the exit of the fairing were used in conjunction with the exit area to obtain the mass flow and the exit velocity.

Bleed zone 3.—Zone 3 was adjacent to zones 2 and 4. Boundary layer air was removed from all four walls of the inlet and diverted to the base region of the airplane through ducts (fig. 7). The mass flow in zone 3 was determined by static pressure measurements made in long tube-shaped ducts near the rear of the airplane. These ducts were calibrated and instrumented so that the airflow could be determined from the pressure loss in the tubes. Exit velocities were determined by using the static pressures measured in the base region, the mass flow, and the exit base area. The drag calculation for zone 3 is the momentum loss only, since the pressure in this region was charged to the base drag component of the airplane drag.

Bleed zone 4.—Zone 4 was between zones 2 and 3. Boundary layer air was removed through porous sections in the floor, outboard side, and ceiling of the inlet. The air from this zone, which made up the smallest component of the total bleed airflow, was discharged overboard through louvers located underneath the inlet on each side of the bleed dump fairing (fig. 5). The drag calculation for this component utilized the exit flow area of the louvers and assumed that the flow through the louvers was choked (had an exit Mach number of 1). The pressure used was the compartment pressure, which was assumed to be the same as the total pressure of the flow, since the Mach number of the airflow in this region was very low.

APPENDIX B.—DERIVATION OF EQUATIONS USED TO DETERMINE LIFT AND DRAG COEFFICIENTS FROM FLIGHT DATA

Before the equations used for the airplane's lift and drag coefficients can be derived, lift and drag must be defined and the coordinate reference systems used must be explained.

For the purposes of this report, airplane lift is defined as the sum of the aerodynamic forces that act on the external surfaces of the aircraft normal to the flightpath and in an upward direction. Airplane drag is defined as the sum of the aerodynamic forces that act on the external surfaces of the aircraft tangential to the flightpath and opposite to the direction of flight. It does not include the components of drag due to the propulsion system as defined in the body of the report.

The coordinate systems are shown schematically in figure 35 along with the forces that act on the airplane in steady flight. The origins of the axes are assumed

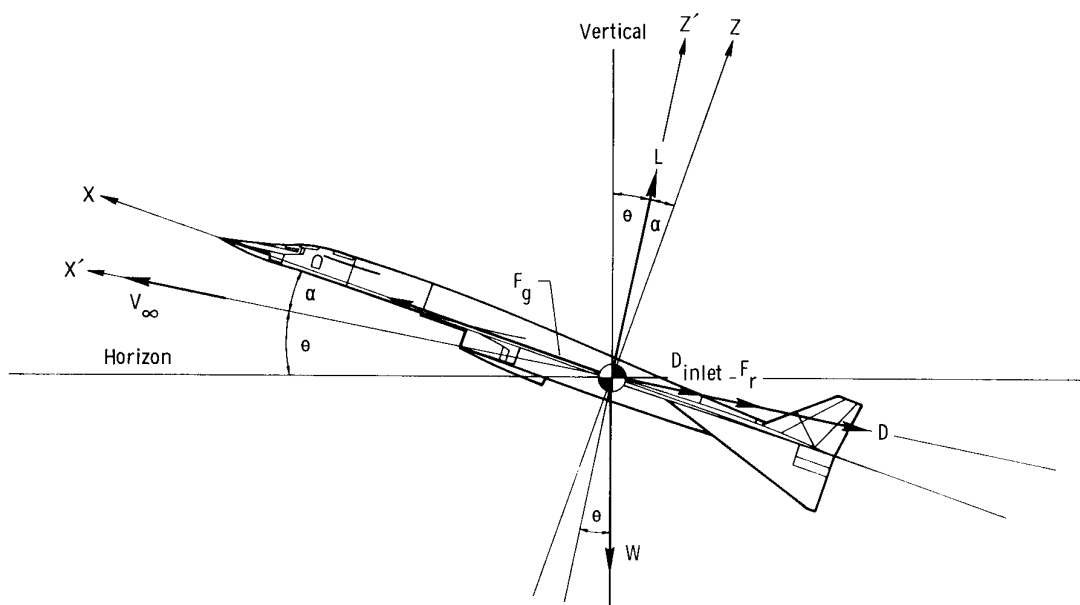


Figure 35. Coordinate system and forces used to derive equations for lift and drag coefficients.

to be the airplane's center of gravity, with the positive directions as indicated. The X - and Z -axes are the airplane body axes; the X -axis is along the fuselage and the Z -axis is normal to the X -axis. The X' - and Z' -axes are the flightpath axes; the X' -axis is tangential to the flightpath and the Z' -axis is normal to it. The relationships of these axes to the horizon are included in the figure.

APPENDIX B.—Continued

The following equation was used to add the forces in the direction of the X' -axis:

$$F_g \cos \alpha - D - (D_{inlet} + F_r) - W \sin \theta = \frac{W}{g} a_{X'}$$

Solving for drag,

$$D = F_g \cos \alpha - (D_{inlet} + F_r) - W \sin \theta - \frac{W}{g} a_{X'}$$

The following equation was used to add the forces in the direction of the Z' -axis:

$$L - W \cos \theta + F_g \sin \alpha = \frac{W}{g} a_{Z'}$$

Solving for lift,

$$L = W \cos \theta - F_g \sin \alpha + \frac{W}{g} a_{Z'}$$

Since airplane acceleration was sensed along the X - and Z -axes, lift and drag had to be expressed in terms of acceleration along these axes. The relationship between acceleration along the X' - and Z' -axes and along the X - and Z -axes is as follows (fig. 36):

$$a_{X'} = a_X \cos \alpha - a_Z \sin \alpha$$

$$a_{Z'} = a_Z \cos \alpha + a_X \sin \alpha$$

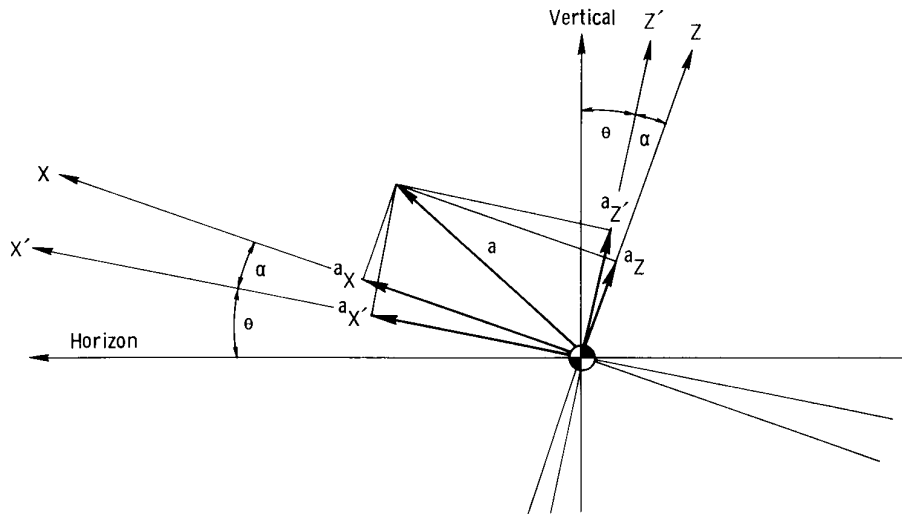


Figure 36. Relationship of airplane accelerations in different coordinate systems.

APPENDIX B.—Continued

The accelerometers along the X - and Z -axes measured both the acceleration of the airplane and the component due to gravity along these axes. The normal acceleration, or component due to gravity, is a function of the angle $\theta + \alpha$. The accelerometer output is in g 's, and it is related to a_X and a_Z as follows:

$$n_X = \frac{a_X}{g} + \sin (\theta + \alpha)$$

$$n_Z = \frac{a_Z}{g} + \cos (\theta + \alpha)$$

where n_X and n_Z are accelerometer readouts. By using trigonometric identities with the equations above, the following expressions can be obtained for $a_{X'}$ and $a_{Z'}$ in terms of n_X and n_Z :

$$a_{X'} = g(n_X \cos \alpha - n_Z \sin \alpha - \sin \theta)$$

$$a_{Z'} = g(n_Z \cos \alpha + n_X \sin \alpha - \cos \theta)$$

The following equations result if these expressions are substituted into the equations for lift and drag:

$$D = W(n_Z \sin \alpha - n_X \cos \alpha) + F_g \cos \alpha - (D_{inlet} + F_r)$$

$$L = W(n_Z \cos \alpha + n_X \sin \alpha) - F_g \sin \alpha$$

The coefficients for lift and drag are defined as follows:

$$C_D = \frac{D}{q_\infty S_w}$$

$$C_L = \frac{L}{q_\infty S_w}$$

where q_∞ is free-stream dynamic pressure ($0.5 \gamma p_\infty M_\infty^2$), and S_w is airplane wing reference area (585 square meters (6297 square feet)).

Solving the lift and drag equations in terms of the coefficients results in the following expressions:

$$C_D = \frac{1}{q_\infty S_w} W(n_Z \sin \alpha - n_X \cos \alpha) + F_g \cos \alpha - (D_{inlet} + F_r)$$

APPENDIX B.—Concluded

$$C_L = \frac{1}{q_\infty S_w} W (n_Z \cos \alpha + n_X \sin \alpha) - F_g \sin \alpha$$

The equations above are the general expressions of the lift and drag coefficients. The equations were modified for this study to make them consistent with the definition of net propulsive thrust, F_{nt} , and to permit them to accommodate changes in inlet mass flow from a nominal schedule (fig. 12).

Net propulsive thrust, F_{nt} , is defined as follows (app. A):

$$F_{nt} = F_g - (F_r + D_{inlet})$$

This expression was substituted into the equation for drag coefficient. Changes in inlet mass flow were allowed for by using a drag increment, $\Delta C_{D,mf}$, that was obtained from wind tunnel data.

Thus, the expressions finally used to reduce the flight data were as follows:

$$C_D = \frac{1}{q_\infty S_w} \left[W (n_Z \sin \alpha - n_X \cos \alpha) + F_{nt} - F_g (1 - \cos \alpha) \right] + \Delta C_{D,mf}$$

$$C_L = \frac{1}{q_\infty S_w} \left[W (n_Z \cos \alpha + n_X \sin \alpha) - F_g \sin \alpha \right]$$

REFERENCES

1. Wykes, John H.; and Lawrence, Robert E.: Estimated Performance and Stability and Control Data for Correlation With XB-70-1 Flight Test Data. NASA CR-114335, 1971.
2. Mechtly, E. A.: The International System of Units — Physical Constants and Conversion Factors. NASA SP-7012, 1973.
3. Arnaiz, Henry H.; and Schweikhard, William G.: Validation of the Gas Generator Method of Calculating Jet-Engine Thrust and Evaluation of XB-70-1 Airplane Engine Performance at Ground Static Conditions. NASA TN D-7028, 1970.
4. General Electric Company Model Specification YJ93-GE-3 Engine — Specification No. E-757 F. Flight Propulsion Div., General Electric, Feb. 9, 1959.
5. Edwards, E. L.: An Airborne Data Acquisition System for Use in Flight Testing the XB-70 Airplane. Selected Instrumentation Application Papers From AGARD Flight Mechanics Panel — Twenty-Sixth Meeting, AGARD Rept. 507, June 1965, pp. 23-48.
6. Edwards, E. L.: A Data Processing Facility for the XB-70 Flight Test Program. Flight Test Instrumentation, AGARD Conf. Proc. No. 32, 1967, pp. 243-258.
7. Ince, D. B.: Application Experience With the B-70 Flight Test Data System. Aerospace Instrumentation. Vol. 4 — Proceedings of the Fourth International Aerospace Symposium, College of Aeronautics, Cranfield, Eng., Mar. 21-24, 1966, M. A. Perry, ed., Pergamon Press, Ltd., 1967, pp. 195-208.
8. Webb, Lannie D.; and Washington, Harold P.: Flight Calibration of Compensated and Uncompensated Pitot-Static Airspeed Probes and Application of the Probes to Supersonic Cruise Vehicles. NASA TN D-6827, 1972.
9. Arnaiz, Henry H.: Techniques for Determining Propulsion System Forces for Accurate High Speed Vehicle Drag Measurements in Flight. AIAA Paper 75-964, 1975.
10. Beaulieu, Warren; Campbell, Ralph; and Burcham, William: Measurement of XB-70 Propulsion Performance Incorporating the Gas Generator Method. J. Aircraft, vol. 6, no. 4, July-Aug. 1969, pp. 312-317.
11. Wolowicz, Chester H.; Strutz, Larry W.; Gilyard, Glenn B.; and Matheny, Neil W.: Preliminary Flight Evaluation of the Stability and Control Derivatives and Dynamic Characteristics of the Unaugmented XB-70-1 Airplane Including Comparisons With Predictions. NASA TN D-4578, 1968.

12. Saltzman, Edwin J.; Goecke, Sheryll A.; and Pembo, Chris: Base Pressure Measurements on the XB-70 Airplane at Mach Numbers From 0.4 to 3.0. NASA TM X-1612, 1968.
13. Shapiro, Ascher H.: The Dynamics and Thermodynamics of Compressible Fluid Flow. Vol. I. The Ronald Press Co., c.1953.
14. Ames Research Staff: Equations, Tables, and Charts for Compressible Flow. NACA Rept. 1135, 1953.

TABLE 1.—GEOMETRIC CHARACTERISTICS OF XB-70 AIRPLANES

Total wing —		
Total area (includes 230.62 m ² (2482.34 ft ²) covered by fuselage but not 3.12 m ² (33.53 ft ²) of the wing ramp area), m ² (ft ²)	585.07 (6297.8)	
Span, m (ft)	32 (105)	
Aspect ratio	1.751	
Taper ratio	0.019	
	<u>XB-70-1</u>	<u>XB-70-2</u>
Dihedral angle, deg	0	5
Root chord (wing station 0), m (ft)	35.89 (117.76)	
Tip chord (wing station 16 m (630 in.)), m (ft)	0.67 (2.19)	
Mean aerodynamic chord (wing station 5.43 m (17.82 ft)), m (ft)	23.94 (78.532)	
Fuselage station of 25-percent wing mean aerodynamic chord, m (ft)	41.18 (135.10)	
Sweepback angle, deg:		
Leading edge	65.57	
25-percent element	58.79	
Trailing edge	0	
Incidence angle, deg:		
Root (fuselage juncture)	0	
Tip (fold line and outboard)	-2.60	
Airfoil section (modified hexagonal):		
Root to wing station 4.72 m (186 in.) (thickness-chord ratio, 2 percent)	0.30 to 0.70	
Wing station 11.68 m (460 in.) to 16.00 m (630 in.) (thickness-chord ratio, 2.5 percent)	0.30 to 0.70	
Inboard wing —		
Area (includes 230.62 m ² (2482.34 ft ²) covered by fuselage but not 3.12 m ² (33.53 ft ²) wing ramp area), m ² (ft ²)	488.28 (5256.0)	
Span, m (ft)	19.34 (63.44)	
Aspect ratio	0.766	
Taper ratio	0.407	
	<u>XB-70-1</u>	<u>XB-70-2</u>
Dihedral angle, deg	0	5
Root chord (wing station 0), m (ft)	35.89 (117.76)	
Tip chord (wing station 9.67 m (380.62 in.)), m (ft)	14.61 (47.94)	
Mean aerodynamic chord (wing station 4.15 m (163.58 in.)), m (in.)	26.75 (1053)	
Fuselage station of 25-percent wing mean aerodynamic chord, m (in.)	39.07 (1538.29)	
Sweepback angle, deg:		
Leading edge	65.57	
25-percent element	58.79	
Trailing edge	0	

TABLE 1.—Continued

Airfoil section (modified hexagonal):		
Root (thickness-chord ratio, 2 percent)		0.30 to 0.70
Tip (thickness-chord ratio, 2.4 percent)		0.30 to 0.70
Mean camber (leading edge), deg:		
Butt plane 0		0.15
Butt plane 2.72 m (107 in.)		4.40
Butt plane 3.89 m (153 in.)		2.75
Butt plane 6.53 m (257 in.)		2.60
Butt plane 9.32 m (367 in.) to tip		0
Outboard wing —		
Area (one side only), m ² (ft ²)	48.39 (520.90)	
Span, m (ft)	6.33 (20.78)	
Aspect ratio	0.829	
Taper ratio	0.046	
Dihedral angle, deg	5	
Root chord (wing station 9.67 m (380.62 in.)), m (ft)	14.61 (47.94)	
Tip chord (wing station 16.00 m (630 in.)), m (ft)	0.67 (2.19)	
Mean aerodynamic chord (wing station 11.87 m (467.37 in.)), m (in.)	9.76 (384.25)	
Sweepback angle, deg:		
Leading edge	65.57	
25-percent element	58.79	
Trailing edge	0	
Airfoil section (modified hexagonal):		
Root (thickness-chord ratio, 2.4 percent)	0.30 to 0.70	
Tip (thickness-chord ratio, 2.5 percent)	0.30 to 0.70	
	<u>XB-70-1</u>	<u>XB-70-2</u>
Down deflection from wing reference		
plane, deg	0, 25, 65	0, 30, 70
Skewline of tip fold, deg:		
Leading edge in		1.5
Leading edge down		3
	<u>Up</u>	<u>Wingtips</u> <u>Down</u>
Elevons (data for one side):		
Total area aft of hinge line, m ² (ft ²)	18.37 (197.7)	12.57 (135.26)
Span, m (ft)	6.23 (20.44)	4.26 (13.98)
Inboard chord (equivalent), m (in.)	2.95 (116)	2.95 (116)
Outboard chord (equivalent), m (in.)	2.95 (116)	2.95 (116)
Sweepback angle of hinge line, deg	0	0
Deflection, deg:		
As elevator		-25 to 15
As aileron with elevators at ±15° or less		-15 to 15
As aileron with elevators at -25°		-5 to 5
Total		-30 to 30

TABLE 1.—Continued

Canard —

Area (includes 13.96 m ² (150.31 ft ²) covered by fuselage), m ² (ft ²)	38.61 (415.59)
Span, m (ft)	8.78 (28.81)
Aspect ratio	1.997
Taper ratio	0.388
Dihedral angle, deg	0
Root chord (canard station 0), m (ft)	6.34 (20.79)
Tip chord (canard station 4.39 m (172.86 in.)), m (ft)	2.46 (8.06)
Mean aerodynamic chord (canard station 1.87 m (73.71 in.)), m (in.)	4.68 (184.3)
Fuselage station of 25-percent canard mean aerodynamic chord, m (in.)	14.06 (553.73)
Sweepback angle, deg:	
Leading edge	31.70
25-percent element	21.64
Trailing edge	-14.91
Incidence angle (nose up), deg	0 to 6
Airfoil section (modified hexagonal):	
Root (thickness-chord ratio 2.5 percent)	0.34 to 0.66
Tip (thickness-chord ratio 2.52 percent)	0.34 to 0.66
Ratio of canard area to wing area	0.066
Canard flap (one of two):	
Area (aft of hinge line), m ² (ft ²)	5.08 (54.69)
Ratio of flap area to canard semiaarea	0.263

Vertical tail (one of two) —

Area (includes 0.83 m ² (8.96 ft ²) blanketed area), m ² (ft ²)	21.74 (233.96)
Span, m (ft)	4.57 (15)
Aspect ratio	1
Taper ratio	0.30
Root chord (vertical-tail station 0), m (ft)	7.03 (23.08)
Tip chord (vertical-tail station 4.57 m (180 in.)), m (ft)	2.11 (6.92)
Mean aerodynamic chord (vertical-tail station 1.88 m (73.85 in.)), m (in.)	5.01 (197.40)
Fuselage station of 25-percent vertical-tail mean aerodynamic chord, m (in.)	55.59 (2188.50)
Sweepback angle, deg:	
Leading edge	51.77
25-percent element	45
Trailing edge	10.89
Airfoil section (modified hexagonal):	
Root (thickness-chord ratio 3.75 percent)	0.30 to 0.70
Tip (thickness-chord ratio 2.5 percent)	0.30 to 0.70
Cant angle, deg	0
Ratio of vertical-tail to wing area	0.037

TABLE 1.—Continued

Rudder travel, deg:	
With gear extended	±12
With gear retracted	±3
Fuselage (includes canopy) —	
Length, m (ft)	56.62 (185.75)
Maximum depth (fuselage station 22.30 m (878 in.)), m (in.)	2.72 (106.92)
Maximum breadth (fuselage station 21.72 m (855 in.)), m (in.)	2.54 (100)
Side area, m ² (ft ²)	87.30 (939.72)
Planform area, m ² (ft ²)	110.07 (1184.78)
Center of gravity:	
Forward limit, percent mean aerodynamic chord	19.0
Aft limit, percent mean aerodynamic chord	25.0
Duct —	
Length, m (ft)	31.96 (104.84)
Maximum depth (fuselage station 34.93 m (1375 in.)), m (in.)	2.31 (90.75)
Maximum breadth (fuselage station 53.34 m (2100 in.)), m (in.)	9.16 (360.70)
Side area, m ² (ft ²)	66.58 (716.66)
Planform area, m ² (ft ²)	217.61 (2342.33)
Inlet captive area (each), m ² (in ²)	3.61 (5600)
Surface areas (net wetted), m ² (ft ²) —	
Fuselage, canopy, boundary layer gutter, and tailpipes	264.77 (2850.0)
Duct	318.71 (3430.6)
Wing, wingtips, and wing ramp	864.71 (9307.7)
Vertical tails (two)	87.12 (937.7)
Canard	49.47 (532.5)
Total	1584.79 (17,058.5)
Engines (six)	YJ93-GE-3
Boattail angle, deg —	
Upper surface	6
Lower surface	5
Side	6
Base areas, m ² (ft ²) —	
Total	12.7 (137)
Total (all engines on, minimum exit area)	10 (107.2)
Total (all engines on, maximum exit area)	4.5 (48.5)
Projected thickness (height) of base, m (in.)	1.47 (58)
Width of propulsion package, cm (in.)	914 (360)

TABLE 1.—Concluded

Linear dimension pertinent to orifices, cm (in.) —	
Orifices 1, 3, 4, 6, 7, 8, 9, 10, 11	161 (63.5)
Orifices 2 and 5	29 (11.5)
Engine —	
Jet-exit area (minimum), cm ² (in ²)	4613 (715)
Jet-exit area (maximum), cm ² (in ²)	13,678 (2120)
Jet-exit diameter (minimum), cm (in.)	77 (30.2)
Jet-exit diameter (maximum), cm (in.)	132 (52)

TABLE 2.—RANGE AND ACCURACY OF SENSORS USED FOR MEASUREMENTS
USED IN CALCULATING INLET DRAG COMPONENTS

(a) Free-stream conditions

Type of measurement	Sensor range	Accuracy, percent of full range
Static pressure	0 to 13,800 N/m ² (0 to 20 lb/in ²)	Figure 8
Total temperature —		
Low range	213 to 433 K (385 to 785 °R)	1.2
High range	423 to 643 K (760 to 1160 °R)	1.2

(b) Inlet bypass door system

Type of measurement	Sensor range	Accuracy, percent of full range
Bypass door position, all doors	0° to 19°	2
Bypass air total pressure, left side only	±6900 N/m ² (±10 lb/in ²)	2

(c) Boundary layer bleed system

Type of measurement	Sensor range, N/m ² (lb/in ²)	Accuracy, percent of full range
Inlet diverter —		
Total pressure	±4100 (±6)	2
Static pressure	±4100 (±6)	2
Zone 1 —		
Total pressure	±4100 (±6)	2
Static pressure	±2800 (±4)	2
Zone 2 —		
Total pressure	±4100 (±6)	2
Static pressure	±4100 (±6)	2
Zone 3 —		
Static pressure, forward	±4100 (±6)	2
Static pressure, aft	±4100 (±6)	2
Zone 4 static pressure	±6900 (±10)	2

TABLE 3.—ESTIMATED UNCERTAINTY IN MEASURED
PERFORMANCE PARAMETERS

Parameter	Uncertainty	
	XB-70-1	XB-70-2
M_{∞}	Figure 8	Figure 8
p_{∞}	Figure 8	Figure 8
α , deg	0.3	0.3
n_X , g	0.0025	0.0035
n_Z , g	0.020	0.025
W , percent	1.5	2.0
F_{nt} , percent	5	6
F_g , percent	3	4

TABLE 4.—SUMMARY OF THE XB-70 FLIGHT CONDITIONS AND THE PERFORMANCE
AND CONFIGURATION PARAMETERS MEASURED IN FLIGHT

(a) Flight conditions

Data point number	Airplane	M_∞	Altitude, m (ft)	T_{t_∞} , K (°R)	q_∞ , N/m ² (lb/ft ²)	Aircraft rate of climb, m/min (ft/min)
^a 1	XB-70-1	0.759	7,842 (25,730)	267 (482)	14,684 (306.7)	0 (0)
2		0.758	7,727 (25,460)	268 (483)	14,823 (309.6)	108 (360)
3		0.757	7,763 (25,580)	267 (482)	14,703 (307.1)	456 (1,500)
4		0.740	7,887 (25,990)	265 (478)	13,803 (288.3)	564 (1,860)
5		0.741	7,839 (25,830)	265 (478)	13,933 (291.0)	-420 (-1,380)
6		0.773	7,745 (25,520)	268 (484)	15,369 (321.0)	-492 (-1,620)
7		0.762	7,745 (25,520)	268 (483)	14,943 (312.1)	0 (0)
8		0.721	7,930 (26,130)	263 (475)	13,018 (271.9)	1,404 (4,620)
9	XB-70-1	0.926	9,939 (32,750)	276 (498)	15,877 (331.6)	0 (0)
10		0.933	9,939 (32,750)	276 (498)	16,154 (337.4)	-36 (-120)
^a 11		0.930	9,988 (32,770)	276 (498)	16,030 (334.8)	72 (240)
12		0.913	9,954 (32,800)	275 (496)	15,426 (322.2)	90 (300)
13		0.915	10,149 (33,440)	273 (493)	15,043 (314.2)	-180 (-600)
14		0.948	9,806 (32,310)	278 (502)	17,016 (355.4)	-474 (-1,560)
15		0.927	9,924 (32,700)	276 (498)	15,987 (333.9)	252 (840)
^b 16		0.938	10,294 (33,920)	274 (494)	15,460 (322.9)	294 (960)
^b 17		0.940	10,960 (33,960)	274 (494)	15,494 (323.6)	-474 (-1,560)
18	XB-70-1	1.049	8,083 (26,520)	303 (546)	27,100 (566.0)	234 (780)
19		1.049	8,159 (26,770)	302 (545)	27,162 (567.3)	0 (0)
^a 20		1.058	8,272 (27,140)	302 (545)	26,813 (560.0)	0 (0)
21		1.062	8,275 (27,150)	303 (547)	27,004 (564.0)	36 (120)
22		1.066	8,243 (27,160)	303 (547)	27,191 (567.9)	72 (260)
23		1.061	8,607 (28,360)	298 (538)	25,534 (533.3)	0 (0)
24		1.014	10,142 (33,420)	267 (482)	18,488 (386.1)	36 (120)
25		1.063	9,672 (31,870)	277 (499)	21,840 (456.2)	-36 (-120)
26	XB-70-1	1.105	9,860 (32,490)	285 (514)	22,929 (478.9)	0 (0)
27		1.115	9,857 (32,480)	286 (515)	23,359 (487.9)	0 (0)
28		1.122	9,842 (32,430)	286 (516)	23,712 (495.2)	-90 (-30)
^a 29	XB-70-1	1.175	10,278 (33,720)	296 (534)	24,478 (511.3)	-378 (-1,260)
30		1.175	10,194 (33,590)	297 (535)	24,624 (514.3)	-366 (-1,200)
31		1.170	10,009 (32,980)	298 (537)	25,132 (524.9)	726 (2,400)
^a 32		1.153	10,400 (34,121)	293 (529)	23,130 (483.1)	0 (0)
^a 33		1.172	10,046 (32,960)	298 (538)	25,323 (527.0)	-108 (-360)
^b 34		1.175	10,136 (33,400)	297 (536)	24,849 (519.0)	-1,656 (-5,460)
^b 35		1.183	10,124 (33,360)	298 (538)	25,242 (527.2)	1,074 (3,540)
36		1.187	9,787 (32,250)	284 (512)	26,764 (559.0)	-54 (-180)
37		1.205	9,782 (32,230)	286 (515)	27,602 (576.5)	-72 (-240)
38	XB-70-1	1.626	12,567 (41,410)	325 (585)	32,457 (677.9)	-72 (-240)
39		1.625	12,574 (41,430)	326 (588)	32,357 (675.8)	126 (420)
40		1.647	12,546 (41,340)	329 (593)	33,384 (697.3)	0 (0)
41		1.653	12,574 (41,430)	330 (594)	33,481 (699.3)	216 (720)
^a 42		1.671	12,807 (42,020)	331 (596)	33,260 (694.7)	0 (0)
43		1.679	12,810 (42,210)	331 (596)	33,276 (695.0)	-126 (-420)
44		1.671	12,841 (42,310)	331 (597)	32,810 (685.3)	180 (600)
45		1.692	12,701 (41,850)	333 (600)	34,379 (718.0)	90 (300)
46		1.595	11,721 (38,620)	313 (563)	35,685 (745.3)	0 (0)
^a 47		1.608	11,756 (38,570)	315 (567)	36,355 (759.3)	0 (0)

^a Airplane deformations determined.

^b Acquired from climb/descent maneuver.

TABLE 4.—Continued

(a) Concluded

Data point number	Airplane	M_∞	Altitude, m (ft)	T_{t_∞} , K (°R)	q_∞ , N/m ² (lb/ft ²)	Aircraft rate of climb, m/min (ft/min)
^a 48	XB-70-1	2.151	17,563 (57,620)	400 (720)	26,037 (543.8)	0 (0)
49		2.157	17,490 (57,630)	400 (720)	26,166 (546.5)	0 (0)
50		2.146	17,499 (57,660)	398 (717)	25,869 (540.3)	0 (0)
51		2.197	17,788 (58,610)	412 (742)	25,883 (540.6)	330 (1,080)
^a 52		2.100	14,813 (48,600)	396 (713)	38,297 (799.8)	0 (0)
53		2.105	14,744 (48,580)	395 (711)	38,508 (804.3)	-18 (-60)
54		2.125	14,789 (48,730)	396 (714)	38,956 (816.6)	-36 (-120)
55		2.103	14,628 (48,200)	395 (712)	39,147 (817.6)	180 (600)
56		2.092	14,731 (48,540)	394 (710)	38,107 (795.9)	1,710 (5,640)
57		2.104	14,744 (48,580)	394 (710)	38,472 (803.5)	0 (0)
58	XB-70-1	2.375	17,163 (56,550)	462 (832)	33,405 (697.7)	0 (0)
59		2.375	17,184 (56,620)	463 (834)	33,310 (695.7)	0 (0)
60		2.375	17,227 (56,760)	463 (834)	32,998 (689.2)	0 (0)
61	XB-70-1	2.491	19,041 (62,740)	473 (853)	27,305 (570.3)	1,332 (4,380)
62		2.494	19,411 (63,960)	476 (858)	25,807 (539.0)	0 (0)
63		2.500	18,650 (61,450)	471 (848)	29,264 (611.2)	-18 (-60)
64		2.515	18,650 (61,450)	470 (847)	29,613 (618.5)	0 (0)
65		2.490	19,220 (63,330)	463 (834)	26,515 (553.8)	-----
66		2.522	19,008 (62,630)	467 (842)	28,139 (587.7)	-528 (-1,740)
67		2.491	18,382 (60,570)	450 (811)	30,303 (632.9)	-984 (-3,240)
^b 68		2.512	18,983 (62,550)	477 (860)	28,024 (585.3)	1,728 (5,700)
69		2.517	19,351 (63,760)	476 (857)	26,539 (554.3)	1,146 (3,780)
^b 70		2.543	18,999 (62,600)	473 (853)	28,651 (598.4)	-1,440 (-4,740)
71		2.506	19,093 (62,910)	478 (861)	27,406 (572.4)	198 (660)
^a 72		2.526	19,187 (62,950)	480 (864)	27,801 (580.6)	18 (60)
73		2.498	19,247 (63,420)	472 (851)	26,583 (555.2)	180 (600)
74		2.523	19,257 (63,450)	472 (850)	27,076 (565.5)	-72 (-240)
75		2.513	18,604 (61,300)	475 (856)	29,781 (622.0)	894 (2,940)
76		2.524	19,093 (62,910)	476 (857)	27,799 (580.6)	-256 (-840)
77		2.527	19,090 (62,900)	475 (856)	27,885 (582.4)	0 (0)
78		2.525	19,090 (62,900)	476 (857)	27,620 (581.5)	0 (0)
^a 79		2.505	19,205 (63,010)	476 (857)	27,257 (569.3)	366 (1,200)
80		2.543	19,217 (63,320)	480 (864)	27,679 (578.1)	-330 (-1,080)
81		2.569	19,160 (63,160)	482 (868)	28,469 (594.6)	-528 (-1,740)
^a 82		2.564	19,224 (63,070)	482 (868)	28,468 (594.6)	-618 (-2,040)
83		2.520	19,232 (63,370)	481 (867)	27,114 (566.3)	1,056 (3,480)
84		2.477	19,081 (62,870)	478 (861)	26,836 (560.5)	618 (2,040)
85		2.481	19,108 (62,960)	477 (860)	26,798 (559.7)	-18 (-60)
^a 86		2.498	18,784 (61,630)	480 (865)	28,966 (605.0)	-18 (-60)
87		2.493	18,780 (61,614)	481 (867)	28,910 (603.8)	36 (120)
88		2.503	18,842 (62,085)	481 (866)	28,450 (594.2)	1,038 (3,420)
89		2.519	18,735 (61,730)	482 (869)	29,307 (612.1)	-654 (-2,160)
90		2.484	18,842 (62,085)	477 (860)	28,000 (584.8)	1,002 (3,300)
91	XB-70-2	2.770	19,858 (65,430)	514 (926)	29,676 (619.8)	0 (0)
92		2.764	21,217 (69,910)	542 (976)	23,818 (497.5)	0 (0)
93		2.789	21,047 (69,350)	550 (990)	24,920 (520.5)	0 (0)
94		2.776	21,096 (69,510)	547 (984)	24,492 (511.5)	0 (0)
95	XB-70-2	2.977	21,499 (70,840)	491 (1,063)	26,448 (552.4)	-108 (-360)
96		2.979	21,445 (70,660)	594 (1,070)	26,713 (557.9)	-54 (-180)
97		3.001	21,624 (71,250)	593 (1,067)	26,326 (549.8)	-90 (-300)
98		2.982	21,499 (70,840)	594 (1,069)	26,537 (554.3)	0 (0)
99		3.065	21,830 (71,930)	596 (1,073)	26,615 (555.9)	0 (0)

^a Airplane deformations determined.^b Acquired from climb/descent maneuver.

TABLE 4. —Continued
(b) Performance parameters and airplane configurations

Data point number	F_{nt} , N (lb)	F_g , N (lb)	W, N (lb)	α_{meas} , deg	n_z , g	n_x , g	δ_c , deg	δ_e , deg	δ_a , deg	δ_l , deg		δ_r , deg		Center of gravity, percent mean aerodynamic chord
										Left	Right	Left	Right	
a ₁	158,944 (35,734)	261,337 (58,754)	1,406,012 (318,394)	4.3	1.02	0.0803	2.26	2.7	0.2	-1.0	-0.5	0.1	-0.2	24.1
2	163,477 (36,753)	266,920 (60,009)	1,416,287 (314,100)	4.1	0.97	0.0849	2.26	2.7	0.4	-1.0	-0.5	0	-0.2	23.4
3	161,204 (36,242)	264,913 (59,558)	1,396,227 (313,900)	5.0	1.22	0.0893	2.43	2.5	0.6	-1.3	-0.4	0.2	-0.2	23.4
4	159,127 (35,775)	256,507 (57,668)	1,396,004 (313,850)	3.0	0.59	0.0804	1.92	3.1	0.1	-0.1	-0.1	-0.1	0	23.4
5	159,216 (35,785)	257,766 (57,951)	1,396,004 (313,850)	3.7	0.80	0.0839	2.03	3.2	0.2	-1.1	-0.1	0	-0.1	23.4
6	163,263 (36,705)	269,642 (60,621)	1,395,782 (313,800)	5.7	1.47	0.0934	2.69	1.6	-0.2	-1.3	-0.7	0.3	-0.3	23.3
7	162,614 (36,559)	265,527 (59,696)	1,395,782 (313,800)	5.8	1.50	0.0949	2.71	1.4	-0.5	-1.3	-0.7	0.2	-0.4	23.3
8	156,800 (35,252)	249,857 (56,173)	1,395,204 (313,670)	4.6	0.94	0.0910	2.24	2.5	0.5	-1.2	-0.2	0.1	-0.1	23.2
9	240,063 (53,971)	347,455 (78,115)	2,123,030 (477,300)	5.6	1.02	0.1024	2.15	2.6	0.3	23.1	24.8	0.5	-0.1	22.2
10	240,338 (54,033)	349,341 (78,539)	2,101,680 (472,500)	5.9	1.08	0.1033	2.21	2.5	1.3	23.0	24.8	0.6	-0.1	22.2
a ₁₁	240,441 (54,056)	348,425 (78,333)	2,136,525 (480,310)	5.5	1.02	0.1026	2.15	2.4	1.1	23.0	24.7	0.6	-0.1	21.9
12	235,810 (53,015)	339,925 (76,422)	2,107,462 (473,800)	6.8	1.24	0.1100	2.43	1.5	0.3	23.0	24.8	0.6	-0.2	22.2
13	235,926 (53,041)	340,085 (76,458)	2,103,904 (473,300)	4.3	0.70	0.0964	1.91	3.1	1.0	23.5	25.3	0.4	0.3	22.2
14	250,440 (56,304)	366,319 (82,356)	2,101,012 (472,350)	7.2	1.51	0.1100	2.68	0.7	0.5	22.4	24.4	0.6	-0.3	22.3
15	240,178 (53,997)	348,282 (78,301)	2,095,897 (471,200)	5.8	1.05	0.1039	2.15	2.6	2.6	22.7	24.8	0.5	-0.3	22.3
b ₁₆	304,745 (68,513)	408,117 (91,753)	2,175,072 (489,000)	5.9	1.00	0.1360	2.05	2.6	1.2	23.0	24.8	0.6	-0.1	22.6
b ₁₇	198,265 (44,574)	305,030 (68,577)	2,146,160 (482,500)	5.9	1.01	0.0770	2.15	2.5	1.3	23.2	24.8	0.6	-0.1	22.2
18	436,442 (98,121)	622,564 (139,965)	1,941,552 (436,500)	3.8	0.98	0.0700	---	---	---	---	---	---	---	21.8
19	434,640 (97,716)	618,663 (139,088)	1,926,873 (433,200)	3.8	0.99	0.0700	---	---	---	---	---	---	---	21.8
a ₂₀	431,109 (96,922)	614,962 (138,256)	1,943,761 (436,975)	3.8	1.00	0.0700	0.51	12.4	---	24.0	24.0	---	---	22.3
21	431,411 (96,980)	616,817 (138,673)	1,891,734 (425,300)	3.7	0.99	0.0700	---	---	---	---	---	---	---	22.3
22	432,172 (97,161)	618,721 (139,101)	1,885,952 (424,000)	3.7	1.00	0.0700	---	---	---	---	---	---	---	22.3
23	419,410 (94,292)	595,066 (133,733)	1,859,264 (418,000)	3.9	1.00	0.0780	---	---	---	---	---	---	---	22.2
24	353,078 (79,378)	478,822 (107,649)	2,099,456 (472,000)	5.0	1.00	0.1065	1.39	7.9	2.3	21.0	24.2	0.4	-0.5	20.0
25	392,696 (88,286)	547,041 (122,986)	2,068,320 (465,000)	4.5	1.00	0.0943	1.17	9.8	2.2	20.6	24.2	0.4	-0.7	21.8
26	385,739 (86,722)	546,196 (122,796)	2,070,544 (465,500)	5.1	1.07	0.0950	1.38	8.4	-1.0	20.1	24.0	0.6	0.1	21.6
27	389,671 (87,606)	553,002 (124,326)	2,068,320 (465,000)	5.1	1.07	0.0960	1.24	8.8	0.4	20.1	23.4	0.5	0.3	21.6
28	393,505 (88,468)	559,376 (125,759)	2,066,096 (464,500)	4.9	1.04	0.0960	1.32	7.0	1.1	20.1	23.8	0.6	0.3	21.6

^a Airplane deformations determined.

^b Acquired from climb/descent maneuver.

TABLE 4.—Continued
(b) Continued

Data point number	F_{nt} , N (lb)	F_g , N (lb)	W , N (lb)	α , meas ^a , deg	n_2 , g	n_X , g	δ_c , deg	δ_e , deg	δ_a , deg	δ_t , deg		δ_r , deg		Center of gravity, percent mean aerodynamic chord
										Left	Right	Left	Right	
a ₂₉	328,898 (73,943)	499,448 (112,286)	1,532,190 (344,450)	3.1	1.02	0.0500	0.90	10.4	----	23.8	25.3	0.1	0.3	22.3
30	329,476 (74,073)	500,649 (112,556)	1,498,976 (337,000)	3.1	1.02	0.0480	-----	-----	-----	23.2	24.8	-----	-----	21.8
31	352,757 (79,307)	527,901 (118,683)	1,486,521 (334,200)	3.7	1.28	0.0740	-----	-----	-----	23.2	24.7	-----	-----	21.5
a ₃₂	333,390 (74,953)	493,994 (111,060)	1,521,513 (342,050)	2.2	0.66	0.0436	0.41	12.8	-----	23.2	24.7	-----	-----	21.5
a ₃₃	351,151 (78,946)	523,760 (117,752)	1,517,955 (341,250)	4.3	1.51	0.0880	1.61	6.8	-----	23.2	24.8	-----	-----	21.0
b ₃₄	249,056 (55,993)	421,901 (94,852)	1,561,248 (351,000)	3.0	0.91	-0.0200	1.05	11.3	0.9	24.0	25.6	0.2	0.5	20.8
b ₃₅	381,522 (85,774)	556,124 (125,028)	1,550,128 (348,500)	3.1	0.98	0.0870	0.99	10.6	1.0	23.6	25.2	0.1	0.4	21.6
36	385,214 (86,604)	575,873 (129,468)	1,541,232 (346,500)	3.3	1.02	0.0705	0.85	10.4	1.1	21.5	24.7	-0.2	0	21.5
37	377,412 (84,850)	580,815 (130,579)	1,525,664 (343,000)	3.1	1.00	0.0611	0.82	10.8	1.1	21.5	25.0	-0.1	0	21.7
38	366,212 (82,332)	633,488 (142,421)	1,705,363 (383,400)	3.3	1.06	0.0773	1.40	8.2	2.4	63.9	64.1	0.1	0.5	21.3
39	370,522 (82,060)	587,300 (132,037)	1,701,804 (382,600)	3.2	1.02	0.0474	1.34	8.8	-0.5	64.1	64.1	0.1	0.6	21.3
40	376,741 (84,699)	649,408 (146,000)	1,672,892 (376,100)	2.9	1.00	0.0730	1.28	10.6	0.6	62.2	64.1	-0.3	-0.3	22.1
41	377,822 (84,942)	652,441 (146,682)	1,672,003 (375,900)	3.1	1.09	0.0760	1.44	9.5	1.2	63.2	65.7	-0.5	-0.3	22.1
a ₄₂	347,735 (78,178)	626,038 (140,746)	1,673,865 (376,300)	2.9	1.00	0.0620	1.38	9.3	1.6	64.9	67.2	-0.4	-0.1	22.0
43	346,984 (78,009)	624,605 (140,424)	1,632,416 (367,000)	3.6	1.26	0.0780	1.76	7.0	1.6	61.1	63.1	-0.3	-0.3	22.0
44	342,576 (77,018)	615,865 (138,459)	1,630,192 (366,500)	1.9	0.67	0.0560	1.03	7.1	1.1	61.8	63.7	-0.5	-0.1	22.0
45	354,078 (79,604)	645,440 (145,108)	1,627,968 (366,000)	3.9	1.43	0.0850	1.95	6.1	2.1	60.8	62.9	-0.2	-0.3	22.0
46	371,923 (83,616)	669,139 (150,436)	1,753,401 (394,200)	3.0	1.00	0.0546	1.11	10.0	-0.1	60.0	63.8	-0.3	-0.2	21.8
a ₄₇	386,144 (86,813)	690,885 (155,325)	1,779,751 (400,104)	3.0	1.00	0.0619	1.14	9.7	1.1	60.0	63.7	-0.4	0.1	21.7
a ₄₈	240,365 (54,039)	482,358 (108,444)	1,572,602 (353,535)	4.4	1.05	0.0612	2.59	3.7	3.2	63.4	61.7	-0.8	-0.1	21.1
49	240,921 (54,164)	480,610 (108,051)	1,543,456 (347,000)	4.3	1.02	0.0620	2.59	3.9	1.0	63.4	61.6	-0.7	-0.2	22.0
50	240,707 (54,116)	483,648 (108,734)	1,547,904 (348,000)	4.1	0.96	0.0607	2.43	5.4	1.0	63.6	61.4	-0.8	0	22.0
51	279,023 (62,730)	529,031 (118,937)	1,765,856 (397,000)	4.9	1.02	0.0736	2.49	5.1	-0.5	62.7	62.2	-0.5	0	22.2
a ₅₂	322,377 (72,477)	682,269 (153,388)	1,745,522 (392,409)	3.1	1.00	0.0620	1.98	6.2	0.1	60.8	63.8	-0.5	0	21.1
53	326,727 (73,455)	690,151 (155,160)	1,717,817 (386,200)	3.0	1.00	0.0640	2.03	6.1	0	61.1	63.7	-0.5	0	21.2
54	327,128 (73,545)	697,473 (156,806)	1,715,816 (385,750)	2.0	0.69	0.0536	1.56	8.5	0.5	61.3	63.8	-0.5	0.1	21.1
55	329,378 (74,051)	697,032 (156,707)	1,714,259 (385,400)	c _{4.5}	1.41	0.0760	2.55	2.6	1.7	60.5	63.3	-0.3	-0.1	21.0
56	324,717 (73,003)	682,741 (153,494)	1,713,369 (385,200)	2.3	0.75	0.0600	1.66	7.5	0.5	61.2	63.8	-0.4	-0.3	21.0
57	324,494 (72,953)	687,482 (154,560)	1,716,928 (386,000)	3.7	1.20	0.0720	2.28	4.1	1.5	60.7	63.1	-0.4	-0.1	21.0
58	297,749 (66,940)	633,235 (142,364)	1,661,328 (373,500)	4.2	1.04	0.0820	-----	-----	-----	-----	-----	-----	-----	21.6
59	297,193 (66,815)	630,686 (141,791)	1,658,214 (372,800)	4.4	1.09	0.0860	-----	-----	-----	-----	-----	-----	-----	21.6
60	293,536 (65,993)	625,873 (140,709)	1,654,656 (372,000)	3.9	0.97	0.0780	-----	-----	-----	-----	-----	-----	-----	21.6

^aAirplane deformations determined.

^bAcquired from climb/descent maneuver.

^cEstimated.

TABLE 4.—Concluded
(b) Concluded

Data point number	F_{nt} , N (lb)	F_g , N (lb)	W , N (lb)	α_{meas} , deg	η_z , g	η_X , g	δ_c , deg	δ_e , deg	δ_a , deg	δ_t , deg		δ_r , deg		Center of gravity, percent mean aerodynamic chord
										Left	Right	Left	Right	
61	288,426 (64,844)	599,305 (134,736)	1,639,088 (368,500)	4.6	0.99	0.1046	2.85	2.8	1.7	63.5	61.9	-0.3	0.9	21.9
62	195,058 (43,853)	486,851 (109,454)	1,636,964 (368,000)	5.0	0.99	0.0540	2.89	2.5	0.8	63.8	61.7	-0.4	0.8	21.6
63	247,455 (55,633)	581,593 (130,754)	1,632,432 (371,500)	4.5	1.00	0.0751	2.89	2.5	2.5	63.5	61.9	-0.5	0.7	22.3
64	249,586 (56,112)	588,230 (132,246)	1,641,312 (369,000)	4.6	1.03	0.0750	2.82	2.9	1.7	63.5	61.9	-0.4	0.8	22.3
65	233,493 (52,494)	532,060 (119,618)	1,556,800 (350,000)	4.4	0.93	0.0786	2.88	2.7	2.4	63.7	61.8	-0.4	0.8	21.5
66	244,186 (54,898)	560,794 (126,078)	1,552,352 (349,000)	4.8	1.09	0.0799	2.91	2.8	1.1	64.0	61.5	-0.3	0.9	21.8
67	113,739 (25,571)	440,743 (99,088)	1,494,528 (336,000)	3.9	0.99	-0.0240	2.79	3.3	1.2	64.2	60.7	-0.5	0.7	20.5
b ⁶⁸	279,587 (62,857)	599,198 (134,712)	1,770,304 (398,000)	c ⁴ .7	0.94	0.0983	2.49	3.3	2.4	63.1	63.3	-0.6	-0.1	22.7
69	266,017 (59,806)	567,222 (127,523)	1,767,190 (397,300)	c ⁵ .1	0.96	0.0926	2.55	2.8	2.5	62.9	63.3	-0.5	0.1	22.6
b ⁷⁰	175,989 (39,566)	502,552 (112,984)	1,751,177 (393,700)	c ⁴ .7	0.97	0.0327	2.58	2.7	1.9	63.0	63.4	-0.5	0.1	22.1
71	217,413 (48,879)	524,534 (117,926)	1,659,104 (373,000)	c ⁴ .7	0.96	0.0643	2.80	3.2	1.9	63.6	63.1	-0.6	0.2	21.6
a ⁷²	221,301 (49,753)	532,167 (119,642)	1,674,827 (376,516)	c ⁴ .7	0.98	0.0640	2.82	3.2	2.0	63.9	62.9	-0.7	0.2	21.8
73	214,736 (48,277)	511,871 (115,079)	1,645,760 (370,000)	c ⁴ .6	0.93	0.0589	2.76	3.8	1.5	63.8	62.7	-0.6	0.2	21.9
74	221,314 (49,756)	527,412 (118,573)	1,641,312 (369,000)	c ⁵ .0	1.03	0.0580	2.84	3.3	2.2	64.0	62.8	-0.7	0.2	22.0
75	292,616 (65,786)	621,025 (139,619)	1,732,496 (389,500)	c ⁴ .7	1.01	0.0986	2.64	3.3	2.1	63.1	63.4	-0.5	0	21.9
76	276,176 (62,090)	588,826 (132,380)	1,587,936 (357,000)	c ⁴ .7	1.03	0.0950	3.12	1.9	2.8	64.2	62.5	-0.8	0.2	20.4
77	275,753 (61,995)	588,701 (132,352)	1,586,601 (356,700)	c ⁵ .3	1.17	0.1083	3.41	-0.3	2.1	64.2	62.3	-0.7	0.2	20.4
78	274,486 (61,710)	587,136 (132,000)	1,586,156 (356,600)	c ⁵ .6	1.24	0.1014	3.55	-1.4	2.8	64.2	62.4	-0.7	0.2	20.4
a ⁷⁹	271,861 (61,102)	577,265 (129,781)	1,608,103 (361,516)	c ³ .7	0.81	0.0957	2.70	4.6	0.6	64.2	62.5	-0.8	0.3	20.5
80	274,045 (61,611)	587,763 (132,141)	1,583,488 (356,000)	c ⁴ .0	0.88	0.0964	2.89	4.0	1.4	64.3	62.5	-0.7	0.3	20.4
81	284,138 (63,880)	607,143 (136,498)	1,582,153 (355,700)	c ⁶ .0	1.38	0.1093	3.90	-3.6	3.1	64.0	62.3	-0.7	0	20.4
a ⁸²	284,538 (63,970)	608,833 (136,878)	1,604,990 (360,816)	c ⁶ .6	1.50	0.1077	4.07	-5.2	3.8	64.0	62.2	-0.6	0.1	20.5
83	266,599 (59,937)	571,483 (128,481)	1,579,929 (355,200)	4.5	0.96	0.0995	3.03	2.4	1.5	64.2	62.4	-0.7	0.4	20.4
84	191,695 (43,097)	476,896 (107,216)	1,694,688 (381,000)	4.8	0.95	0.0470	2.81	1.8	2.3	61.1	63.2	-0.5	0.1	21.0
85	227,617 (51,173)	511,391 (114,971)	1,691,574 (380,300)	4.9	0.98	0.0681	2.92	0.8	1.8	61.3	63.4	-0.2	0.5	21.0
a ⁸⁶	270,558 (60,827)	578,324 (130,019)	1,697,401 (381,591)	4.6	1.00	0.0867	2.76	3.0	0.3	61.1	63.2	-0.3	0.4	21.6
87	271,021 (60,931)	577,848 (129,912)	1,688,972 (375,200)	5.5	1.19	0.0870	3.08	0.6	1.3	61.1	63.1	-0.3	0.3	21.3
88	268,392 (60,340)	574,219 (129,096)	1,667,110 (374,800)	3.0	0.64	0.0820	2.09	7.8	-0.2	61.6	63.2	-0.3	0.5	21.4
89	271,154 (60,961)	583,880 (131,268)	1,664,886 (374,300)	6.5	1.47	0.0970	3.53	-2.1	1.3	61.1	63.1	-0.2	0.4	21.5
90	255,364 (57,411)	548,113 (123,227)	1,661,772 (373,600)	4.4	0.89	0.0820	2.53	4.9	0.5	61.4	63.2	-0.1	0.7	21.6
91	222,915 (50,116)	568,503 (127,811)	1,631,014 (366,685)	c ⁴ .2	0.99	0.0724	---	---	---	---	---	---	---	---
92	193,003 (43,391)	483,470 (108,694)	1,405,496 (315,984)	4.4	0.98	0.0817	---	---	---	---	---	---	---	23.9
93	190,276 (42,778)	500,279 (112,473)	1,405,497 (319,494)	4.3	0.98	0.0765	2.90	0	-1.6	---	---	-0.3	0.6	22.5
94	198,456 (44,617)	496,441 (111,610)	1,421,087 (319,489)	4.4	0.98	0.0838	2.87	0.3	-1.1	---	---	-0.3	0.6	22.5
95	230,922 (51,916)	571,625 (128,513)	1,573,862 (353,836)	4.6	0.96	0.0901	---	---	---	---	---	---	---	22.0
96	223,761 (50,306)	567,555 (127,598)	1,569,325 (352,816)	4.5	0.97	0.0894	---	---	---	---	---	---	---	22.0
97	225,277 (50,647)	561,884 (126,323)	1,480,187 (332,776)	4.4	0.98	0.0913	3.19	-3.7	1.5	68.1	65.5	-1.4	-0.2	21.3
98	224,361 (50,441)	564,375 (126,883)	1,476,431 (331,936)	4.4	0.98	0.0908	3.22	-3.2	1.3	68.0	65.5	-1.4	-0.1	21.3
99	197,535 (44,410)	527,230 (118,532)	1,457,858 (327,756)	4.5	1.00	0.0774	3.12	-2.6	-0.3	68.0	65.5	-1.3	-0.1	21.5

^aAirplane deformations determined.^bAcquired from climb/descent maneuvers.^cEstimated.